Pre-recombinational energy release and narrow features in the CMB spectrum

J. Chluba[1] and R.A. Sunyaev[1,2]

[1] Max-Planck-Institut für Astrophysik, Karl-Schwarzschild-Str. 1, 85741 Garching bei München, Germany
[2] Space Research Institute, Russian Academy of Sciences, Profsoyuznaya 84/32, 117997 Moscow, Russia

ABSTRACT

Energy release in the early Universe ($z \lesssim 2 \times 10^6$) should lead to some broad spectral distortion of the cosmic microwave background (CMB) radiation field, which can be characterized as y-type distortion when the injection process started at redshifts $z \lesssim 5 \times 10^4$. Here we demonstrate that if energy was released before the beginning of cosmological hydrogen recombination ($z \sim 1400$), closed loops of bound-bound and free-bound transitions in H I and He II lead to the appearance of (i) characteristic multiple narrow spectral features at dm and cm wavelengths, and (ii) a prominent sub-millimeter feature consisting of absorption and emission parts in the far Wien tail of CMB spectrum. The additional spectral features are generated in the pre-recombinational epoch of H I ($z \gtrsim 1800$) and He II ($z \gtrsim 7000$), and therefore differ from those arising due to normal cosmological recombination in the undisturbed CMB blackbody radiation field. We present the results of numerical computations including 25 atomic shells for both H I and He II, and discuss the contributions of several individual transitions in detail. As examples, we consider the case of instantaneous energy release (e.g. due to phase transitions) and exponential energy release because of long-lived decaying particles. Our computations show that due to possible pre-recombinational atomic transitions the variability of the CMB spectral distortion increases when comparing with the distortions arising in the normal recombination epoch. The amplitude of the spectral features, both at low and high frequencies, directly depends on the value of the y-parameter, which describes the intrinsic CMB spectral distortion resulting from the energy release. Also the time-dependence of the injection process play an important role, for example leading to non-trivial shifts of the quasi-periodic pattern at low frequencies along the frequency axis. The existence of these narrow spectral features would open an unique way to separate y-distortions due to pre-recombinational ($1400 \lesssim z \lesssim 5 \times 10^4$) energy release from those arising in the post-recombinational era at redshifts $z \lesssim 800$.

Key words. Cosmic Microwave Background: spectral distortions – Atomic Processes: recombination – Cosmology: theory

1. Introduction

The measurements with the COBE/FIRAS instrument have proven that the spectrum of the cosmic microwave background (CMB) is very close to a perfect blackbody (Fixsen et al. 1996) with thermodynamic temperature $T_0 = 2.725 \pm 0.001$ K (Mather et al. 1999; Fixsen & Mather 2002). However, from the theoretical point of view deviations of the CMB spectrum from the one of a pure blackbody are not only possible but even inevitable if, for example, energy was released in the *early Universe* (e.g. due to viscous damping of acoustic waves, or annihilating or decaying particles). For very early energy release ($5 \times 10^4 \lesssim z \lesssim 2 \times 10^6$) the resulting spectral distortion can be characterized as a Bose-Einstein μ-type distortion (Sunyaev & Zeldovich 1970b; Illarionov & Syunyaev 1975a,b), while for energy release at low redshifts ($z \lesssim 5 \times 10^4$) the distortion is close to a y-type distortion (Zeldovich & Sunyaev 1969). The current best observational limits on these types of distortions are $|y| \leq 1.5 \times 10^{-5}$ and $|\mu| \leq 9.0 \times 10^{-5}$ (Fixsen et al. 1996). Due to the rapid technological development, improvements of these limits by a factor of ~ 50 in principle could have been possible already several years ago (Fixsen & Mather 2002), and recently some efforts are made to determine the absolute value of the CMB brightness temperature at low frequencies using ARCADE (Kogut et al. 2004, 2006).

Also in the *post-recombinational epoch* ($z \lesssim 800$), y-type spectral distortions due to different physical mechanisms should be produced. Performing measurements of the average CMB spectrum (e.g. with wide-angle horns or like it was done with COBE/FIRAS) all clusters of galaxies, hosting hot intergalactic gas, due to the thermal SZ-effect (Sunyaev & Zeldovich 1972b) are contributing to the integral value of the observed y-parameter. Similarly supernova remnants at high redshifts (Oh et al. 2003), or shock waves arising due to large-scale structure formation (Sunyaev & Zeldovich 1972a; Cen & Ostriker 1999; Miniati et al. 2000) should contribute to the overall y-parameter. For its value today we only have the upper limit by COBE/FIRAS, and lower limits derived by estimating the total contribution of all clusters in the Universe (Markevitch et al. 1991; da Silva et al. 2000; Roncarelli et al. 2007). These lower limits are exceeding $y \sim 10^{-6}$, and it is still possible that the contributions to the total value of y due to early energy release are comparable or exceeding those coming from the low redshift Universe.

Several detailed analytical and numerical studies for various energy injection histories and mechanisms can be found in the literature (e.g. Zeldovich & Sunyaev 1969; Sunyaev & Zeldovich 1970b,c,a; Illarionov & Syunyaev 1975a,b; Zeldovich et al. 1972; Chan et al. 1975; Danese & de Zotti 1982; Daly 1991; Burigana et al. 1991b,a, 1995; Hu & Silk 1993a,b; Hu et al. 1994; Salvaterra & Burigana 2002; Burigana & Salvaterra 2003; Chluba & Sunyaev 2004). Two very important conclusions can be drawn from these all

studies: (i) the arising spectral distortions are always *very broad* and practically *featureless*, and (ii) due to the absence of narrow spectral features, distinguishing different injection histories is extremely difficult. This implies that if one would find a *y*-type spectral distortion in the average CMB spectrum, then it is practically impossible to say if the energy injection occurred just before, during or after the epoch of cosmological recombination. In this paper we show that the *pre-recombinational emission* within the bound-bound and free-bound transition of atomic hydrogen and helium should leave multiple *narrow features* ($\Delta\nu/\nu \sim 10 - 30\%$) in the CMB spectrum, that might become observable at cm, dm and sub-mm wavelength (see Sect. 5). This could in principle open a way to directly distinguish pre- and post-recombinational *y*-distortions and even to shed light on the time-dependence of the energy injection process.

At redshifts well before the epoch of He III → He II-recombination ($z \gtrsim 8000$) the total number of CMB photons is not affected by atomic transitions if the intrinsic CMB spectrum is given by a *pure blackbody*. This is because the atomic emission and absorption processes in full thermodynamic equilibrium balance each other. However, a lower redshifts ($z \lesssim 8000$), due to the expansion of the Universe, the medium became sufficiently cold to allow the formation of neutral atoms. The transition to the neutral state is associated with the release of several additional photons per baryon (e.g. ~ 5 photons per hydrogen atom (Chluba & Sunyaev 2006)), even within a pure blackbody ambient CMB radiation field. Refining early estimates (Zeldovich et al. 1968; Peebles 1968; Dubrovich 1975; Dubrovich & Stolyarov 1995, 1997), the spectral distortions arising during hydrogen recombination ($800 \lesssim z \lesssim 1800$), He II → He I-recombination ($1600 \lesssim z \lesssim 3000$), and He III → He II-recombination ($4500 \lesssim z \lesssim 7000$) within a pure blackbody ambient radiation field have been recently computed in detail (Rubiño-Martín et al. 2006; Chluba & Sunyaev 2006; Chluba et al. 2007a; Rubino-Martin et al. 2007). It was also emphasized that measuring these distortions in principle may open another independent way to determine the temperature of the CMB monopole, the specific entropy of the Universe, and the primordial helium abundance, well before the first appearance of stars (e.g. Sunyaev & Chluba 2007; Chluba & Sunyaev 2008; Sunyaev & Chluba 2008).

If on the other hand the intrinsic CMB spectrum deviates from a pure blackbody, full equilibrium is perturbed, and the small imbalance between emission and absorption in atomic transitions can lead to a net change of the number of photons, even prior to the epoch of recombination, in particular owing to *loops* starting and ending in the continuum (Lyubarsky & Sunyaev 1983). These loops are trying to diminish the maximal spectral distortions and are producing several new photons per absorbed one. In this paper we want to demonstrate how the cosmological recombination spectrum is affected if one allows for an intrinsic *y*-type CMB spectral distortion. We investigate the cases of single instantaneous energy injection (e.g. due to phase transitions) and for long-lived decaying particles. There is no principle difficulty in performing the calculations for more general injection histories, also including μ-type distortions, if necessary. However, this still requires a slightly more detailed study, which will be left for a future paper.

In Sect. 2 we provide a short overview regarding the thermalization of CMB spectral distortions after early energy release, and provide formulae which we then use in our computations to describe *y*-type distortions. In Sect. 3 we give explicit expressions for the net bound-bound and free-bound rates in a distorted ambient radiation field. We then derive some estimates

for the expected contributions to the pre-recombinational signals coming from primordial helium in Sect. 4. Our main results are presented in Sect. 5, where we first start by discussing a few simple cases (Sect. 5.1 and 5.2) in order to gain some level of understanding. We support our numerical computations by several analytic considerations in Sect 5.1.1 and Appendix B. In Sect. 5.3 we then discuss the results for our 25 shell computations of hydrogen and He II. First we consider the dependence of the spectral distortions on the value of *y* (Sect. 5.3.1), where Fig. 5 and 6 play the main role. Then in Sects. 5.3.2 and 5.3.3 we investigate the dependence of the spectral distortions on the injection redshift and history, where we are particularly interested in the low frequency variability of the signal (see Fig. 9 and 11). We conclude in Sect. 6.

2. CMB spectral distortions after energy release

After any energy release in the Universe, the thermodynamic equilibrium between matter and radiation in general will be perturbed, and in particular, the distribution of photons will deviate from the one of a pure blackbody. The combined action of Compton scattering, double Compton emission[1] (Lightman 1981; Thorne 1981; Chluba et al. 2007b), and Bremsstrahlung will attempt to restore full equilibrium, but, depending on the injection redshift, might not fully succeed. Using the approximate formulae given in Burigana et al. (1991b) and Hu & Silk (1993a), for the parameters within the concordance cosmological model (Spergel et al. 2003; Bennett et al. 2003), one can distinguish between the following cases for the residual CMB spectral distortions arising from a single energy injection, $\delta\rho_\gamma/\rho_\gamma \ll 1$, at heating redshift z_h:

(I) $z_h < z_y \sim 6.3 \times 10^3$: Compton scattering is *not able* to establish full kinetic equilibrium of the photon distribution with the electrons. Photon producing processes (mainly Bremsstrahlung) can only restore a Planckian spectrum at very low frequencies. Heating results in a Compton *y*-distortion (Zeldovich & Sunyaev 1969) at high frequencies, like in the case of the thermal SZ effect, with *y*-parameter $y \sim \frac{1}{4} \delta\rho_\gamma/\rho_\gamma$.

(II) $z_y < z_h < z_\mu \sim 2.9 \times 10^5$: Compton scattering can establish *partial* kinetic equilibrium of the photon distribution with the electrons. Photons that are produced at low frequencies (mainly due to Bremsstrahlung) diminish the spectral distortion close to their initial frequency, but cannot upscatter strongly. The deviations from a blackbody represent a *mixture* between a *y*-distortion and a μ-distortion.

(III) $z_\mu < z_h < z_{th} \sim 2 \times 10^6$: Compton scattering can establish *full* kinetic equilibrium of the photon distribution with the electrons after a very short time. Low frequency photons (mainly due to double Compton emission) upscatter and slowly reduce the spectral distortion at high frequencies The deviations from a blackbody can be described as a Bose-Einstein distribution with frequency-dependent chemical potential, which is constant at high and vanishes at low frequencies.

(IV) $z_{th} < z_h$: Both Compton scattering and photon production processes are extremely efficient and restore practically any spectral distortion arising after heating, eventually yielding

---

[1] Due to the huge excess in the number of photons over baryons ($N_\gamma/N_b \sim 1.6 \times 10^9$), the double Compton process is the dominant source of new photons at redshifts $z_{dc} \gtrsim 3 \times 10^5 - 4 \times 10^5$, while at $z \lesssim z_{dc}$ Bremsstrahlung is more important.

a pure blackbody spectrum with slightly higher temperature T_γ than before the energy release.

For the case (I) and (III) it is possible to approximate the distorted radiation spectrum analytically. There is no principle difficulty in numerically computing the time-dependent solution for the radiation field after release of energy (e.g. Hu & Silk 1993a) for more general cases, if necessary. However, here we are particularly interested in demonstrating the main difference in the additional radiation appearing due to atomic transitions in hydrogen and helium *before* the actual epoch of recombination, and for late energy release, in which a y-type spectral distortion is formed. We will therefore only distinguish between case (I) and (III), and assume that the transition between these two cases occurs at $z_{\mu,y} \approx z_\mu/4\sqrt{2} \sim 5.1 \times 10^4$, i.e. the redshift at which the energy exchange time scale equals the expansion time scale (Sunyaev & Zeldovich 1980; Hu & Silk 1993a). The effects due to intrinsic μ-type spectral distortions will be left for a future work, so that below we will restrict ourselves to energy injection at redshift $z \lesssim 50000$.

2.1. Compton y-distortion

For energy release at low redshifts the Compton process is no longer able to establish kinetic equilibrium. If the temperature of the radiation is smaller than the temperature of the electrons photons are upscattered. For photons which are initially distributed according to a blackbody spectrum with temperature T_γ, the efficiency of this process is determined by the Compton y-parameter,

$$y = \int \frac{k_B(T_e - T_\gamma)}{m_e c^2} N_e\, \sigma_T\, dl\,, \tag{1}$$

where σ_T is the Thomson cross section, $dl = c\,dt$, N_e the electron number density, and T_e the electron temperature. For $y \ll 1$, the resulting intrinsic distortion in the photon occupation number of the CMB is approximately given by (Zeldovich & Sunyaev 1969)

$$\Delta n_\gamma = y \frac{x\,e^x}{(e^x - 1)^2}\left[x\frac{e^x + 1}{e^x - 1} - 4\right]. \tag{2}$$

Here $x = h\nu/k_B T_\gamma$ is the dimensionless frequency.

For computational reasons it is convenient to introduce the frequency dependent chemical potential resulting from a y-distortion, which can be obtained with

$$\mu(x) = \ln\left(\frac{1 + n_\gamma}{n_\gamma}\right) - x \stackrel{y \ll 1}{\approx} -y\,x\left[x\frac{e^x + 1}{e^x - 1} - 4\right]. \tag{3}$$

Here $n_{pl}(x) = 1/[e^x - 1]$ is the Planckian occupation number, and $n_\gamma = n_{pl} + \Delta n_\gamma$. For $x \to 0$ and $y \ll 1$ one finds $\mu(x) \approx 2xy$, and for $x \gg 1$ one has $\mu(x) \approx -\ln[1 + y\,x^2]$, or $\mu(x) \approx -y\,x^2$ for $1 \ll x \ll \sqrt{1/y}$. Comparing with a blackbody spectrum of temperature T_γ, for $y > 0$ there is a deficit of photons at low frequencies, while there is an excess at high frequencies. In particular, the spectral distortion changes sign at $x_y \sim 3.8$.

2.1.1. Compton y-distortion from decaying particles

If all the energy is released at a single redshift, $z_i \lesssim z_{\mu,y} \sim 50000$, then after a very short time a y-type distortion is formed, where the y-parameter is approximately given by $y \sim \frac{1}{4}\delta\rho_\gamma/\rho_\gamma$.

However, when the energy release is due to decaying unstable particles, which have sufficiently long life-times, t_X, then the CMB spectral distortion will built up as a function of redshift. In this case the fractional energy injection rate is given by $\delta\dot{\rho}_\gamma/\rho_\gamma \propto e^{-t(z)/t_X}/(1 + z)$, so that the time-dependent y-parameter can be computed as

$$y(z) = y_0 \times \frac{\int_z^\infty dz'\, e^{-t(z')/t_X}/H(z')(1 + z')^2}{\int_0^\infty dz'\, e^{-t(z')/t_X}/H(z')(1 + z')^2}\,, \tag{4}$$

where $y_0 = \frac{1}{4}\delta\rho_\gamma/\rho_\gamma$ is related to the total energy release, and $H(z)$ is the Hubble expansion factor. Note that $y(z)$ is a rather steep function of redshift, which strongly rises around the redshift, z_X, at which $t(z) \equiv t_X$.

3. Atomic transitions in a distorted ambient CMB radiation field

3.1. Bound-bound transitions

Using the occupation number of photons, $n_\gamma = 1/[e^{x+\mu} - 1]$, with frequency-dependent chemical potential $\mu(x)$, one can express the net rate connecting two bound atomic states i and j in the convenient form

$$\Delta R_{ij} = p_{ij}\frac{A_{ij}\,N_i\,e^{x_{ij}+\mu_{ij}}}{e^{x_{ij}+\mu_{ij}} - 1}\left[1 - \frac{g_i}{g_j}\frac{N_j}{N_i}\,e^{-[x_{ij}+\mu_{ij}]}\right], \tag{5}$$

where p_{ij} is the Sobolev-escape probability, A_{ij} is the Einstein-A-coefficient of the transition $i \to j$, N_i and g_i are the population and statistical weight of the upper and N_j and g_j of the lower hydrogen level, respectively. Furthermore we have introduced the dimensionless frequency $x_{ij} = h\nu_{ij}/kT_0(1 + z)$ of the transition, where $T_0 = 2.725$ K is the present CMB temperature (Fixsen & Mather 2002), and $\mu_{ij} = \mu(x_{ij})$.

3.2. Free-bound transitions

For the free-bound transitions from the continuum to the bound atomic states i one has

$$\Delta R_{ci} = N_e\,N_c\,\alpha_i - N_i\beta_i\,, \tag{6}$$

where N_c in the case of hydrogen is the number density of free protons, N_p, and the number density for He III nuclei, $N_{\text{He III}}$, in the case of helium. The recombination coefficient, α_i, and photoionization coefficient, β_i, are given by the integrals

$$\alpha_i = \frac{8\pi}{c^2}\,\tilde{f}_i(T_e)\int_{\nu_{ic}}^\infty \frac{\nu^2\,\sigma_i(\nu)\,e^{x+\mu(x)+(x_{ic}-x)/\rho}}{e^{x+\mu(x)} - 1}\,d\nu \tag{7a}$$

$$\beta_i = \frac{8\pi}{c^2}\int_{\nu_{ic}}^\infty \frac{\nu^2\sigma_i(\nu)}{e^{x+\mu(x)} - 1}\,d\nu\,, \tag{7b}$$

Here $x_{ic} = h\nu_{ic}/kT_\gamma$ is the dimensionless ionization frequency, $\rho = T_e/T_\gamma$ is the ration of the photon and electron temperature, σ_i is the photoionization cross-section for the level i, and $\tilde{f}_i(T_e) = \frac{g_i}{2}\left[\frac{h^2}{2\pi m_e kT_e}\right]^{3/2} \approx \frac{g_i}{2}\,4.14 \times 10^{-16}\,T_e^{-3/2}$ cm^3. In full thermodynamic equilibrium the photon distribution is given by a blackbody with $T_\gamma = T_e$. As expected, in this case one finds from Eq. (7) that $\alpha_i^{eq} \equiv \tilde{f}_i(T_e)\,e^{h\nu_{ic}/kT_e}\beta_i^{eq}$.

4. Expected contributions from helium

The number of helium nuclei is only $\sim 8\%$ relative to the number of hydrogen atoms in the Universe. Compared to the radiation coming from hydrogen one therefore naively expects a small addition of photons due to atomic transitions in helium. However, at given frequency the photons due to He II have been released at about $Z^2 = 4$ times higher redshifts than for hydrogen, so that both the number density of particles and temperature of the medium was higher. In addition the expansion of the Universe was faster. As we will show below, these circumstances make the contributions from helium comparable to those from hydrogen, where He II plays a much more important role than He I.

4.1. Contributions due to He II

The speed at which atomic loops can be passed through is determined by the effective recombination rate to a given level i, since the bound-bound rates are always much faster. In order to estimate the contributions to the CMB spectral distortion by He II, we compute the change in the population of level i due to direct recombinations to that level over a very short time interval Δt, i.e. $\Delta N_i \approx N_e\, N_c\, \alpha_i^{\mathrm{He\,II}}\, \Delta t$.

Because *all* the bound-bound transition rates in He II are 16 times larger than for hydrogen, the *relative* importance of the different channels to lower states should remain the same as in hydrogen[2]. Therefore one can assume that the relative number of photons, f_{ij}, emitted in the transition $i \to j$ per additional electron on the level i is like for hydrogen at 4 times lower redshifts.

If we want to know how many of the emitted photons are observed in a fixed frequency interval $\Delta \nu$ today ($z_{\mathrm{obs}} = 0$) we also have to consider that at higher redshift the expansion of the Universe is faster. Hence the redshifting of photons through a given interval $\Delta \nu$ is accomplished in a shorter time interval. For a given transition, these are related by $\Delta t = \frac{1+z}{H(z)\,\nu_{ij}}\,\Delta \nu$. Then the change in the number of photons due to emission in the transition $i \to j$ today should be proportional to

$$\Delta N_\gamma(\nu_{ij}) \sim \frac{f_{ij}(z_{\mathrm{em}})\,\Delta N_i(z_{\mathrm{em}})}{H(z_{\mathrm{em}})\,(1 + z_{\mathrm{em}})^3}\,\frac{(1 + z_{\mathrm{em}})}{\nu_{ij}}\Delta \nu\,, \tag{8}$$

where z_{em} is the redshift of emission, and the change of the volume element due to the expansion of the Universe is taken into account by the factor of $(1 + z_{\mathrm{em}})^3$. This now has to be compared with the corresponding change in the number of photons emitted in the same transition by hydrogen, but at 4 times lower emission redshift.

For hydrogenic atoms with change Z the recombination rate, including stimulated recombination within the ambient CMB blackbody, scales like (Kaplan & Pikelner 1970)

$$\alpha_i \propto \frac{Z^4}{T^{3/2}} \int_{h\nu_i/kT}^{\infty} \frac{\mathrm{d}x}{x^2} \propto \frac{Z^2}{T^{1/2}}\,, \tag{9}$$

where ν_i is the ionization frequency of the level i, T is the temperature of the plasma. It was assumed that $h\nu_i \ll kT$. Therefore one finds $\alpha_i^{\mathrm{He\,II}}(4T)/\alpha_i^{\mathrm{H\,I}}(T) \sim 2$. Assuming radiation domination one also has $H(z)/H(4z) \sim 1/16$. Hence, we find $\Delta N_\gamma^{\mathrm{He\,II}}(\nu_{ij}^{\mathrm{H\,I}}, 4z_{\mathrm{em}})/\Delta N_\gamma^{\mathrm{H\,I}}(\nu_{ij}^{\mathrm{H\,I}}, z_{\mathrm{em}}) \sim 8\% \times 4^3\,2/16 \sim 64\%$. Note that $(1 + z_{\mathrm{em}})/\nu_{ij}^{\mathrm{H\,I}} \equiv (1 + 4z_{\mathrm{em}})/\nu_{ij}^{\mathrm{He\,II}}$. Prior to the epoch of He III $\to$ He II recombination the release of photons by helium is amplified by a factor of ~ 8!

4.2. Contributions due to He I

In the case of neutral helium, the highly excited levels are basically hydrogenic. Therefore one does not expect any amplification of the emission within loops prior to its recombination epoch. Furthermore, the total period during which neutral helium can contribute significantly is limited to the redshift range starting at the end of He III $\to$ He II recombination, say $1600 \lesssim z \lesssim 6000$. Therefore, neutral helium typically will not be active over a large range of redshifts.

Still there could be some interesting features appearing in connection with the fine-structure transitions, which even within the standard computations lead to strong negative features in the He I recombination spectrum (Rubino-Martin et al. 2007). Also the spectrum of neutral helium, especially a high frequencies, is more complicated than for hydrogenic atoms, so that some nontrivial features might arise. We leave this problem for some future work, and focus on the contributions of hydrogen and He II.

5. Results for intrinsic y-type CMB distortions

Here we discuss the results for the changes in the recombination spectra of hydrogen and He II for different values of the y-parameter. Some of the computational details and the formulation of the problem can be found in Appendix A.

5.1. The 2 shell atom

In order to understand the properties of the solution and also to check the correctness of our computations we first considered the results including only a small number of shells. If we take 2 shells into account, we are only dealing with a few atomic transitions, namely the Lyman- and Balmer-continuum, and the Lyman-α line. In addition, one expects that during the recombination epoch of the considered atomic species (here H I or He II) also the 2s-1s-two-photon decay channel will contribute, but very little before that time.

In Fig. 1 we show the spectral distortion, ΔI_ν, including 2 shells into our computations for different transitions as a function of redshift[3]. It was assumed that energy was released in a single injection at $z_i = 50000$, leading to $y = 10^{-5}$. All shown curves were computed using the δ-function approximation for the intensity (for details see Rubiño-Martín et al. 2006). This approximation is not sufficient when one is interested in computing the spectral distortions in frequency space.

Prior to the recombination epoch of the considered species one can find pre-recombinational emission and absorption in the Lyman- and Balmer-continuum, and the Lyman-α line, which would be completely absent for $y = 0$. As expected, during in the pre-recombinational epochs the 2s-1s-two-photon transition is not important. This is because the 2s-1s transition is simply unable to compete with the $\sim 10^8$ times faster Lyman-α transition while it is still optically thin.

Summing the spectral distortions due to the continuua, one finds cancellation of the redshift-dependent emission at a level close to our numerical accuracy (relative accuracy $\lesssim 10^{-4}$ for the spectrum). This is expected because of electron number conservation: in the pre-recombinational epoch the overall ionization state of the plasma is not affected significantly by the small

---

[2] Even the factors due to stimulated emission in the ambient blackbody radiation field are the same!

[3] This is a convenient representation of the spectrum, when one is interested in the time-dependence of the photon release, rather than the observed spectral distortion in frequency space. To obtain the later, one simply has to plot the presented curves as a function of $\nu = \nu_{ij}/(1 + z)$, where ν_{ij} is the restframe frequency of the considered transition.
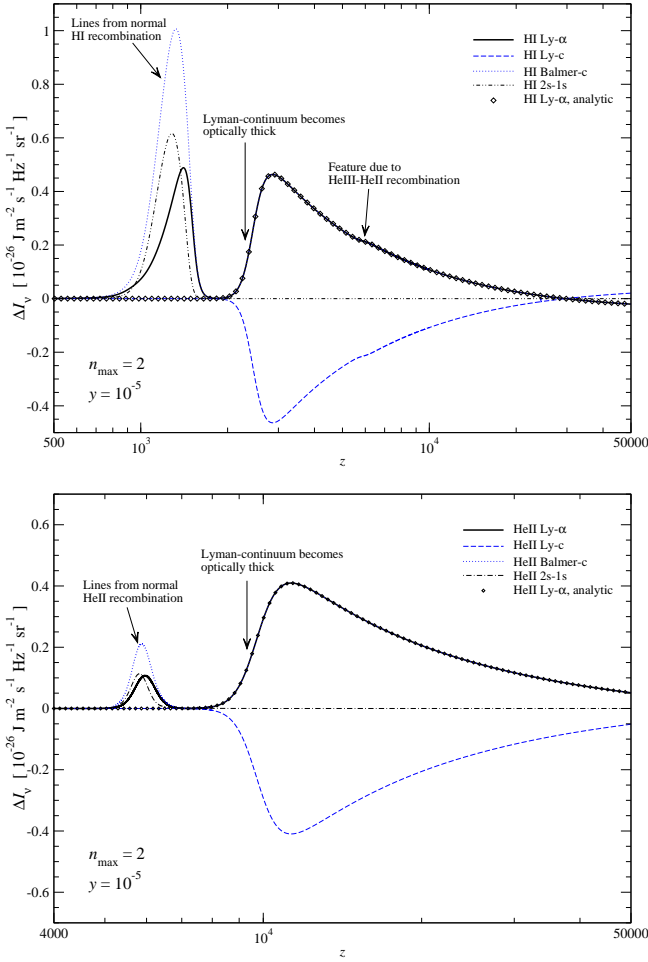
Fig. 1. Spectral distortion, ΔI_ν, including 2 shells into our computations for different transitions as a function of redshift and for $y = 10^{-5}$. All shown curves were computed using the δ-function approximation for the intensity. The upper panel shows the results for hydrogen, the lower those for He II. In both cases the analytic approximation for the Lyman-α line based on Eq. (B.2), and including the escape probabilities in the Lyman-α line and Lyman-continuum, are also shown.
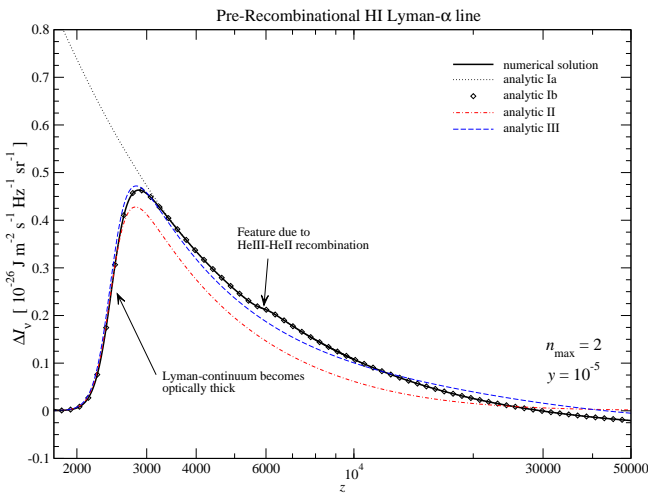
Fig. 2. Analytic representation of the pre-recombinational H I Lyman-α spectral distortions for the 2 shell atom and $y = 10^{-5}$. See text for explanations.

deviations of the background radiation from full equilibrium. Therefore all electrons that enter an atomic species will leave it again, in general via another route to the continuum. This implies that $\sum_i \Delta R_{ci} = 0$, which is a general property of the solution in the pre-recombinational epoch.

If we look at the Lyman- and Balmer-continuum in the case of hydrogen we can see that at redshifts $z \gtrsim 30000$ electrons are entering via the Lyman-continuum, and leaving via the Balmer-continuum, while in the redshift range $2000 \lesssim z \lesssim 30000$ the opposite is true. As expected, for $z \gtrsim 2000$ the Lyman-α transition closely follows the Balmer-continuum, since every electron that enters the 2p-state and then reaches the ground level, had to pass through the Lyman-α transition. Using the analytic solution for the Lyman-α line as given in the Appendix B we find excellent agreement with the numerical results until the real recombination epoch is entered at $z \lesssim 2000$.

In the case of He II for the considered range of redshifts the pre-recombinational emission ($z \gtrsim 7000$) is always generated in the loop $c \rightarrow 2p \rightarrow 1s \rightarrow c$. Again we find excellent agreement with the analytic solution for the Lyman-α line. Note that for He II the total emission in the pre-recombinational epoch is much larger than in the recombination epoch at $z \sim 6000$ (see discussion in Sect. 4). The height of the maximum is even comparable with the H I Lyman-α line.

As one can see from Fig. 1, at high redshifts all transitions become weaker. This is due to the fact that the restframe frequencies of all lines are in the Rayleigh-Jeans part of the CMB spectrum, where the effective chemical potential of the y-distortion (see Sect. 2.1) is dropping like[4] $\mu(x) \approx 2xy$. This implies that at higher redshift all transitions are more and more within a pure blackbody ambient radiation field. On the other hand the effective chemical potential increases towards lower redshift, so that also the strength of the transitions increases. However, at $z \lesssim 3000$ in the case of hydrogen, and $z \lesssim 11000$ for He II, the escape probability in the Lyman-continuum (see Appendix A.1 and Eq. (B.3) for quantitative estimates) starts to decrease significantly, so that the pre-recombinational transitions cease. The maximum in the pre-recombinational Lyman-α line is formed due to this rather sharp transitions to the optically thick region in the Lyman-continuum (see also Sect. 5.1.1 for more details).

5.1.1. Analytic description of the pre-recombinational Lyman-α line

One can understand the behavior of the solution for the spectral distortions in more detail using our analytic description of the Lyman-α line as given in Appendix B.

In Fig. 2 we show the comparison of different approximations with the full numerical result. If we use the analytic approximation based on Eq. (B.2), but do not include the escape probabilities in the H I Lyman-α line and H I Lyman-continuum, then we obtain the dotted curve (quoted 'analytic Ia' in the figure). The curve quoted 'analytic Ib' also includes the escape probabilities as described in Appendix B.1.1. Comparing these curves shows that for the shape of the distortion at $z \lesssim 3000$ the escape probabilities are very important. However, although at this redshift the Sobolev optical depth in the H I Lyman-α line is roughly 14 times larger than the optical depth in the H I Lyman-continuum, the derivation of Eq. (B.8) shows that the H I Lyman-α escape probability only plays a secondary role.

---

[4] Or more correctly $\mu(x) \approx 7.4\,x\,y$ if one also takes into account the difference in the photon and electron temperature $T_e \approx T_\gamma[1 + 5.4\,y]$ (see Appendix A.1).
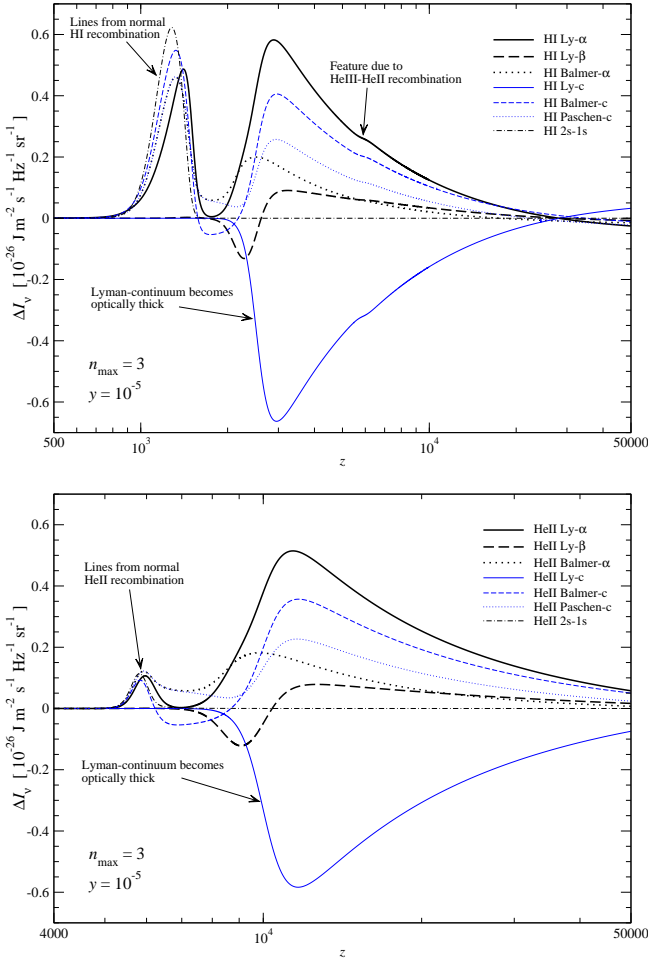
Fig. 4. Sketch of the main atomic loops for hydrogen and He II when including 3 shells. The left panel shows the loops for transitions that are terminating in the Lyman-continuum. The right panel shows the case, when the Lyman-continuum is completely blocked, and unbalanced transitions are terminating in the Balmer-continuum instead.

uum are possible. Looking at Fig. 3 again we find that the sum over all transition in the continuua vanishes at redshifts prior to the actual recombination epoch of the considered species. At $z \lesssim 3000$ in the case of hydrogen, and $z \lesssim 11000$ for He II, the escape probability in the Lyman-continuum becomes small. For 2 shells this fact stopped the pre-recombinational emission until the actual recombination epoch of the considered atomic species was entered (see Fig. 1). However, for 3 shells electrons can now start to leave the 1s-level via the Lyman-β transition, and then reach the continuum through the Balmer-continuum. For both hydrogen and He II one can also see that the emission in the Lyman-α line stops completely, once the Lyman-continuum is fully blocked. In this situation only the loop c $\rightarrow$ 3 $\rightarrow$ 2 $\rightarrow$ c via the Balmer-continuum is working. Only when the main recombinational epoch of the considered species is entered, the Lyman-α line is reactivated.

In Fig. 4 we sketch the main atomic loops in hydrogen and He II when including 3 shells. For $y = 10^{-5}$, in the case of hydrogen the illustrated Lyman-continuum loops work in the redshift range $2000 \lesssim z \lesssim 30000$, while the Balmer-continuum loop works for $1600 \lesssim z \lesssim 2000$. In the case of He II one finds $8000 \lesssim z \lesssim 1.2 \times 10^5$ and $6200 \lesssim z \lesssim 8000$ for the Lyman- and Balmer-continuum loops, respectively. It is clear that in every closed loop one energetic photons is destroyed and *at least* two photons are generated at lower frequencies. Including more shells will open the possibility to generate more photons per loop, simply because electrons can enter through highly excited levels and then preferentially cascade down to the lowest shells via several intermediate levels, leaving the atomic species taking the fastest available route back to the continuum. Below we will discuss this situation in more detail (see Sect. 5.3.1).

Figures 1 and 3 both show that the pre-recombinational lines are emitted in a typical redshift range $\Delta z/z \sim 1$, while the signals from the considered recombinational epoch are released within $\Delta z/z \sim 0.1 - 0.2$. For the pre-recombinational signal the expected line-width is $\Delta \nu/\nu \sim 0.6 - 0.7$. However, the overlap of several lines, especially at frequencies where emission and absorption features nearly coincide, and the asymmetry of the pre-recombinational line profiles, still leads to more narrow spectral features with $\Delta \nu/\nu \sim 0.1 - 0.3$ (see Sect. 5.3, Fig. 6).

It is also important to mention that in all cases the actual recombination epoch is not affected significantly by the small y-distortion in the ambient photon field. There the deviations from Saha-equilibrium because of the recombination dynamics dom-

Fig. 3. Spectral distortion, ΔI_ν, including 3 shells into our computations for different transitions as a function of redshift and for $y = 10^{-5}$. For all shown curves we used the δ-function approximation to compute the intensity. The upper panel shows the results for hydrogen, the lower those for He II.

With the formulae in Appendix B.1.2, the spectral distortion can be written in the form $\Delta I_\nu(z) = F(z) \times \Delta$. If we use F according to Eq. (B.10) and $\Delta \approx \mu_{21} + \mu_{2pc} - \mu_{1sc}$, as derived in Eq. (B.14b), then we obtain the approximation quoted 'analytic II'. One can clearly see that this approximation represents the global behavior, but is fails to explain the Lyman-α absorption at $z \gtrsim 30000$. In fact within this approximation the Lyman-α line should always be in emission, even at very high redshifts, since there $\Delta \approx 3\, y\, x_{1sc}/32 > 0$.

If we also take into account higher order terms for the line imbalance Δ according to Eq. (B.16) then we obtain the curve quoted 'analytic III', which is already very close to the full solution and also reproduces the high redshift behavior, but starting at slightly higher redshift ($z \sim 40000$ instead of $z \sim 30000$). This is largely due to the approximations of the integrals (B.15) over the photoionization cross-sections (in particular M_{-1}). Still if one evaluates these integrals more accurately, one does not recover the full solution, since the free-bound Gaunt-factors were neglected.

5.2. The 3-shell atom

If one takes 3 shells into account, the situation becomes a bit more complicated, since more loops connecting to the contin-
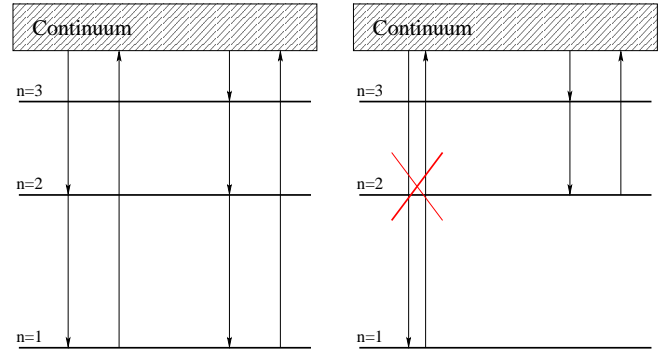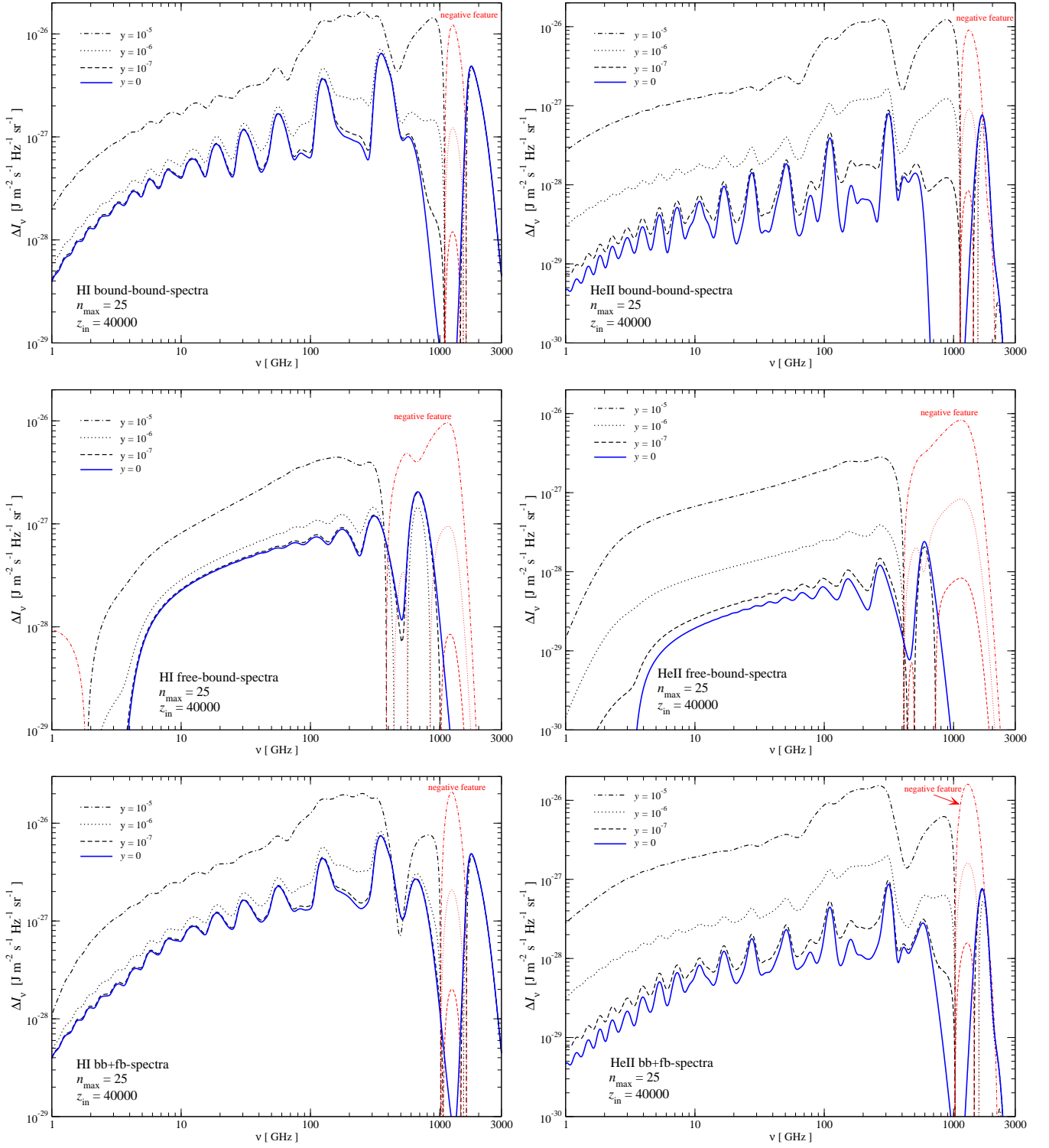
Fig. 5. Contributions to the H I (left panels) and He II (right panels) recombination spectrum for different values of the initial y-parameter. Energy injection was assumed to occur at $z_i = 4 \times 10^4$. In each column the upper panel shows the bound-bound signal, the middle the free-bound signal, and the lower panel the sum of both. The thin red lines represent the overall negative parts of the signals.

inate over those directly related to the spectral distortion, and in particular the changes in the ionization history are tiny.

5.3. The 25-shell atom

In this Section we discuss the results for our 25-shell computations. Given the large amount of transitions, it is better to directly look at the spectral distortion as a function of frequency. However, following the approach of Sect 5.1, we have checked that the basic properties of the first few lines and continuua as a
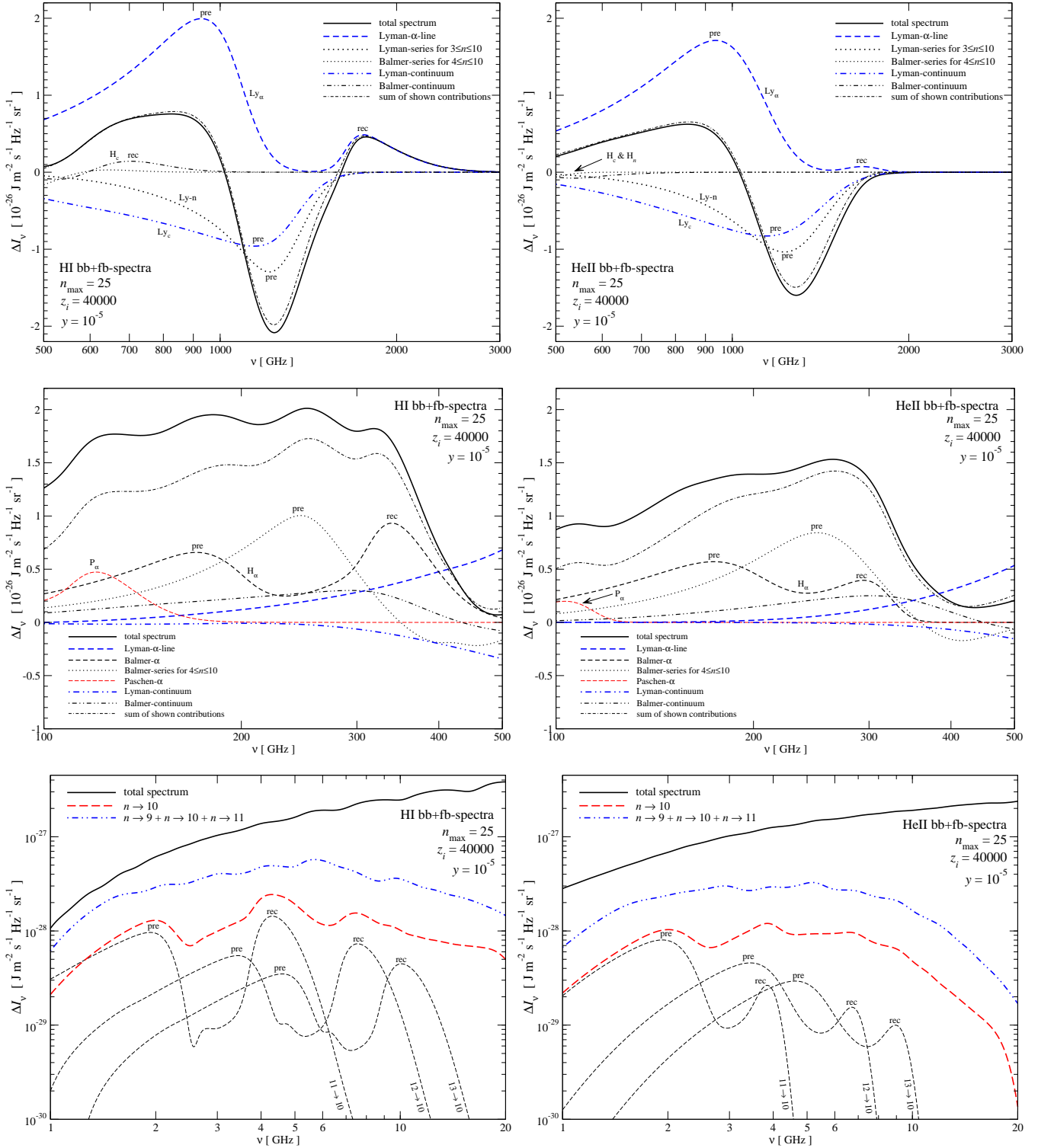
Fig. 6. Main contributions to the H I (left panels) and He II (right panels) spectral distortion at different frequencies for energy injection at $z_i = 40000$ and $y = 10^{-5}$. We have also marked those peaks coming (mainly) from the recombination epoch ('rec') and from the pre-recombination epoch ('pre') of the considered atomic species.

function of redshift do not change qualitatively in comparison to the previous cases. In particular, only the Lyman- and Balmer-continuum become strongly negative, again in similar redshifts ranges as for 2 or 3 shells. In absorption the other continuua play no important role.

Note that for the spectral distortion now the impact of electron scattering has to be considered and the free-bound contribu-

tion must be computed using the full differential photoionization cross section (see Appendix A.4).

5.3.1. Dependence of the distortion on the value of y

In Fig. 5 we show the contributions to the recombination spectrum for different values of the initial y-parameter. In addition,

Fig. 6 shows some of the main contributions to the total hydrogen and He II spectral distortion in more detail.

Bound-bound transitions

Focusing first on the contributions due to bound-bound transitions, one can see that the standard recombination signal due to hydrogen is not very strongly affected when $y = 10^{-7}$, whereas the helium signal already changes notably. Increasing the value of y in both cases leads to an increase in the overall amplitude of the distortion at low frequencies, and a large rise in the emission and variability at $\nu \gtrsim 100$ GHz. For H I at low frequencies the level of the signal changes roughly 5 times when increasing the value of y from 0 to 10^{-5}, while for He II the increase is even about a factor of 40. This shows that in the pre-recombinational epoch He II indeed behaves similar to hydrogen, but with an amplification ~ 8 (see Sect. 4).

At high frequencies, a strong *emission-absorption feature* appears in the range $\nu \sim 500$ GHz $- 1600$ GHz, which is completely absent for $y = 0$. With $y = 10^{-5}$ from peak to peak this feature exceeds the normal Lyman-α distortion (close to $\nu \sim 1750$ GHz for H I and $\nu \sim 1680$ GHz for He II) by a factor of ~ 5 for H I, and about 30 times for He II. The absorption part is mainly due to the pre-recombinational Lyman-β, -γ, and -δ transition, while the emission part is dominated by the pre-recombinational emission in the Lyman-α line (see also Fig. 6 for more detail).

It is important to note that in the case of He II most of the recombinational Lyman-α emission ($\nu \sim 1750$ GHz) is completely wiped out by the pre-recombinational absorption in the higher Lyman-series, while for H I only a very small part of the Lyman-α low frequency wing is affected. This is possible only because the pre-recombinational emission in the He II Lyman-series is so strongly enhanced, as compared to the signal produced during the recombinational epoch.

Free-bound transitions

Now looking at the free-bound contributions, one can again see that the hydrogen signal changes much less with increasing value of y than in the case of He II. In both cases the variability of the free-bound signal decreases at low frequencies, while at high frequencies a strong and broad absorption feature appears, which is mainly due to the Lyman-continuum. For $y = 10^{-5}$ this absorption feature even completely erases the Balmer-continuum contribution appearing during the actual recombination epoch of the considered species. It is 2 times stronger than the H I Lyman-α line from the recombination epoch, and in the case of He II it exceeds the normal He II Lyman-α line by more than one order of magnitude.

However, except for the absorption feature at high frequencies the free-bound contribution becomes practically featureless when reaching $y = 10^{-5}$. This is due to the strong overlap of different lines from the high redshift part, since the characteristic width of the recombinational emission increases like $\Delta\nu/\nu \sim kT_e/h\nu_{ic}$ (see middle panels in Fig. 5). In addition, the photons are released in a more broad range of redshifts (see Sect. 5.1 and 5.2), also leading to a lowering of the contrast of the spectral features from the recombinational epoch.

Table 1. Approximate number of photons and loops per nucleus for $z_i = 4 \times 10^4$ and different values of y.

	$y = 0$	$y = 10^{-7}$	$y = 10^{-6}$	$y = 10^{-5}$
$N_{\mathrm{Ly-c}}^{\mathrm{H\,I}}$	$0 \times N_{\mathrm{H}}$	$-0.028 \times N_{\mathrm{H}}$	$-0.28 \times N_{\mathrm{H}}$	$-2.74 \times N_{\mathrm{H}}$
$N_{\mathrm{Ly-\alpha}}^{\mathrm{H\,I}}$	$0.42 \times N_{\mathrm{H}}$	$0.47 \times N_{\mathrm{H}}$	$0.92 \times N_{\mathrm{H}}$	$5.37 \times N_{\mathrm{H}}$
$N_{\mathrm{bb}}^{\mathrm{H\,I}}$	$2.49 \times N_{\mathrm{H}}$	$2.59 \times N_{\mathrm{H}}$	$3.45 \times N_{\mathrm{H}}$	$12.04 \times N_{\mathrm{H}}$
$\mathcal{N}_{\mathrm{loop}}^{\mathrm{H\,I}}$	$0 \times N_{\mathrm{H}}$	$0.032 \times N_{\mathrm{H}}$	$0.32 \times N_{\mathrm{H}}$	$3.24 \times N_{\mathrm{H}}$
$N_{\mathrm{Ly-c}}^{\mathrm{He\,II}}$	$0 \times N_{\mathrm{He}}$	$-0.27 \times N_{\mathrm{He}}$	$-2.67 \times N_{\mathrm{He}}$	$-26.6 \times N_{\mathrm{He}}$
$N_{\mathrm{Ly-\alpha}}^{\mathrm{He\,II}}$	$0.55 \times N_{\mathrm{He}}$	$1.06 \times N_{\mathrm{He}}$	$5.68 \times N_{\mathrm{He}}$	$51.8 \times N_{\mathrm{He}}$
$N_{\mathrm{bb}}^{\mathrm{He\,II}}$	$2.48 \times N_{\mathrm{He}}$	$3.49 \times N_{\mathrm{He}}$	$12.5 \times N_{\mathrm{He}}$	$103 \times N_{\mathrm{He}}$
$\mathcal{N}_{\mathrm{loop}}^{\mathrm{He\,II}}$	$0 \times N_{\mathrm{He}}$	$0.28 \times N_{\mathrm{He}}$	$2.91 \times N_{\mathrm{He}}$	$30.1 \times N_{\mathrm{He}}$

Total distortion

Also in the total spectra (see lower panels in Fig. 5) one can clearly see a strong absorption feature at high frequencies, which is mainly associated with the Lyman-continuum and Lyman-series for $n > 2$ (see Fig. 6 also). For $y = 10^{-5}$, in the case of hydrogen it exceeds the Lyman-α line from recombination ($\nu \sim 1750$ GHz) by a factor of ~ 4 at $\nu \sim 1250$ GHz, while for He II it is even ~ 20 times stronger, reaching $\sim 80\%$ of the corresponding hydrogen feature. Checking the level of emission at low frequencies, as expected (see Sect. 4), one can find that He II indeed contributes about 2/3 to the total level of emission.

As illustrated in the upper panels of Fig. 6, the emission-absorption feature at high frequencies is due to the overlap of the pre-recombinational Lyman-α line (emission), and the combination of the higher pre-recombinational Lyman-series and Lyman-continuum (absorption). At intermediate frequencies (middle panels), the main spectral features are due to the Balmer-α, pre-recombinational Balmer-series from $n > 3$ and the Paschen-α transition, with some additional broad contributions to the overall amplitude of the bump coming from higher continua.

The lower panels of Fig. 6 show, the separate contributions to the bound-bound series for the 10th shell as an example. One can notice that in the case of hydrogen the recombinational and pre-recombinational emission have similar amplitude, while for He II the pre-recombinational signal is more than one order of magnitude larger (see Sect. 4 for explanation). In both cases the pre-recombinational emission is much broader than the recombinational signal, again mainly due to the time-dependence of the photon emission process (see Sect. 5.1 and 5.2), but to some extent also because of electron scattering.

Number of photons and loops

Using the free-bound spectrum, one can also compute the total number of loops, $\mathcal{N}_{\mathrm{loop}}$, that were involved into the production of photons. This is possible, since only during the recombination epoch electrons will terminate in the 1s-state. Therefore the total number of photons emitted in the free-bound spectrum is very close to $\sim 1\gamma$ per nucleus, while when looking at the positive or negative part of this contribution one should find $\sim (\mathcal{N}_{\mathrm{loop}} + 1)\gamma$ and $\sim -\mathcal{N}_{\mathrm{loop}}\gamma$ per nucleus, respectively.

In Table 1 we give a few examples, also comparing with the number of photons emitted for $y = 0$. One can see that the number of loops per nucleus scales roughly proportional to the values of y, i.e. $\mathcal{N}_{\mathrm{loop}}^{\mathrm{H\,I}} \sim 3.2 \times [y/10^{-5}]$ and $\mathcal{N}_{\mathrm{loop}}^{\mathrm{He\,II}} \sim 30 \times [y/10^{-5}]$. If one would consider a lower injection redshift the proportionality constant should decrease. Also when including more shells $\mathcal{N}_{\mathrm{loop}}$ should become larger. Furthermore, the number of loops
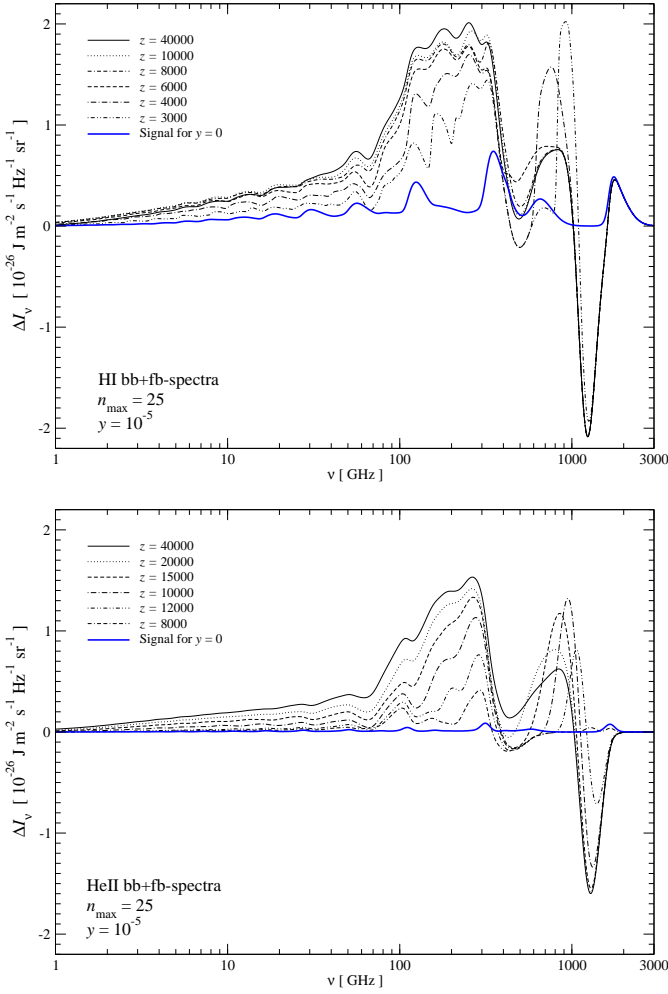
Fig. 7. H I (upper panel) and He II (lower panel) recombination spectra for different energy injection redshifts.

Fig. 8. Total H I + He II recombination spectra for different energy injection redshifts. The upper panel shows details of the spectrum at low, the lower at high frequencies.

per nucleus is about one order of magnitude larger for He II than for hydrogen. As explained in Sect. 4, this is due to the amplification of transitions in the case of hydrogenic helium at high redshifts. Comparing the number of photons absorbed in the Lyman-continuum, one can see that in practically all cases $\sim 90\%$ of all loops are ending there.

If we take the total number of photons per nucleus emitted in the bound-bound transitions and subtract the number of photons emitted for $y = 0$, we can estimate the loop-efficiency, ϵ_{loop}, or number of bound-bound photons generated per loop prior to the recombination epoch. For hydrogen one finds $\epsilon_{loop} \sim 2.9 - 3.1$, while for He II one has $\epsilon_{loop} \sim 3.3 - 3.6$. Similarly one obtains an loop efficiency of $\epsilon_{loop} \sim 1.7 - 1.8$ for both the H I and He II Lyman-α lines. As expected these numbers are rather independent of the value of y, since they should reflect an atomic property. They should also be rather independent of the injection redshift, which mainly affects the total number of loops and thereby the total number of emitted photons. However, the loop efficiency should still increase when including more shells in the computation.

5.3.2. Dependence of the distortion on the redshift of energy injection

To understand how the pre-recombinational emission depends on the redshift at which the energy was released, in Fig. 7 we
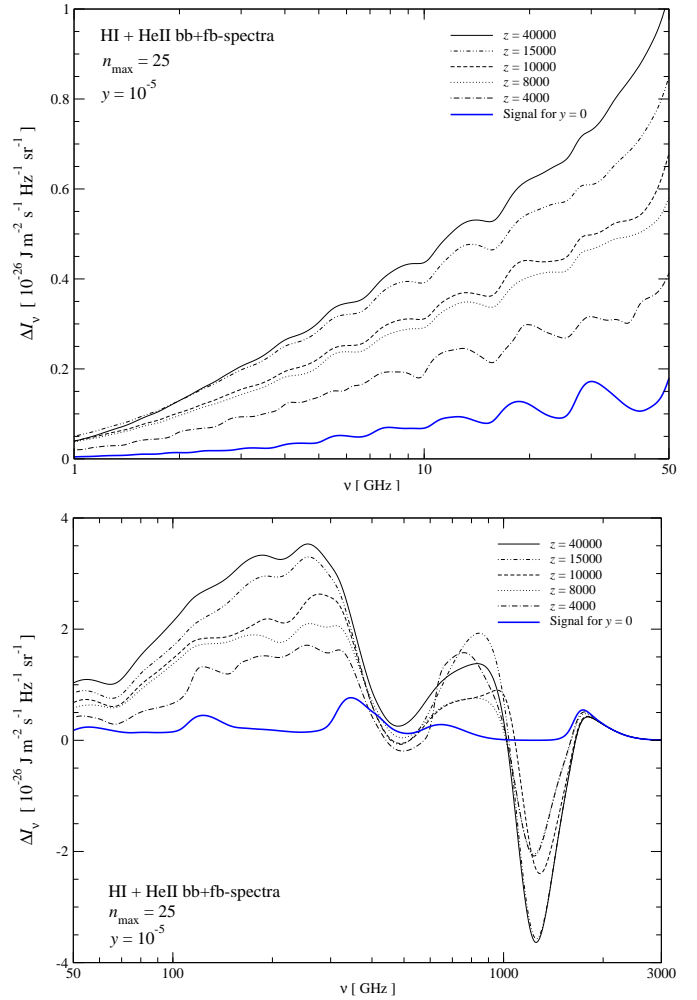
show a compilation of different cases for the total H I and He II signal. In Fig. 8 we also present the sum of both in more detail.

Features at high frequencies

For all shown cases the absolute changes in the curves are strongest at high frequencies ($\nu \gtrsim 100$ GHz). Generally speaking, one can again find a rather broad bump at 100 GHz $\lesssim \nu \lesssim 400$ GHz, followed by an emission-absorption feature in the frequency range 500 GHz $\lesssim \nu \lesssim 1600$ GHz. In particular the strength and position of this emission-absorption feature depends strongly on the redshift of energy injection.

Regarding the broad high-frequency signature, it is more important that the variability is changing, rather than the increase in the overall amplitude. For example, in the frequency range 100 GHz $\lesssim \nu \lesssim 400$ GHz the normal recombinational signal has ~ 2 spectral features, while for injection at $z_i \sim 4000$ roughly 4 features are visible, which in this case only come from hydrogen, since at $z \sim 4000$ He II is already completely recombined. Note that also neutral helium should add some signal, which was not included here. Nevertheless, we expect that this contribution is not strongly amplified like in the case of He II (see Sect. 4), and hence should not add more than $10 - 20\%$ to the total signal.
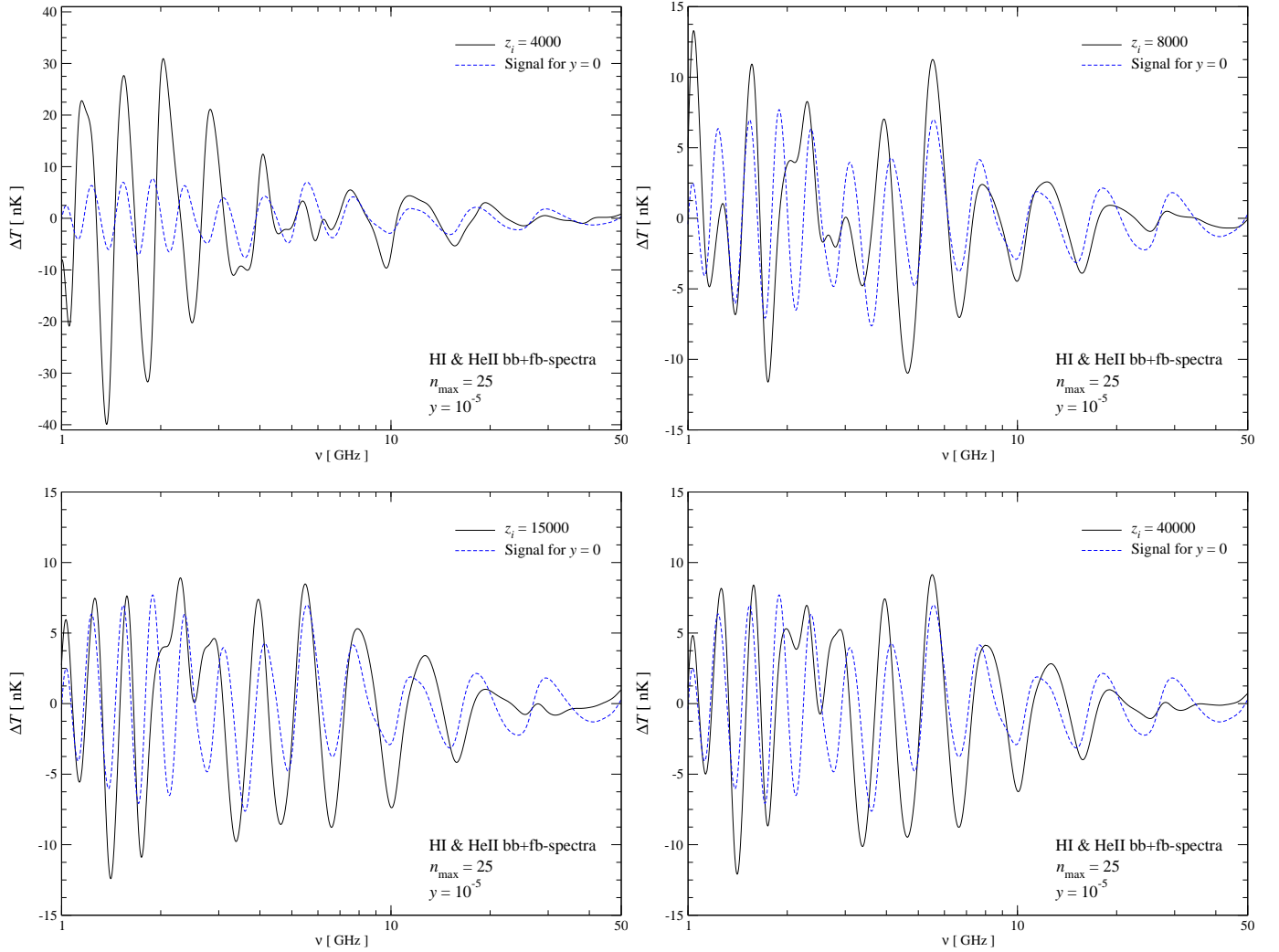
Fig. 9. Comparison of the variable component in the H I + He II bound-bound and free-bound recombination spectra for single energy injection at different redshifts. In all cases the computations were performed including 25 shells and $y = 10^{-5}$. The blue dashed curve in all panel shows the variability in the normal H I + He II recombination spectrum (equivalent to energy injection below $z \sim 800$ or $y = 0$) for comparison.

Variability at low frequencies

Focusing on the spectral distortions at low frequencies, the overall level of the distortion in general increases for higher redshifts of energy release. However, there is also some change in the *variability* of the spectral distortions. In order to study this variability in more detail, in each case we performed a smooth spline fit of the total H I + He II recombination spectrum and then subtracted this curve from the total spectrum. The remaining modulation of the CMB intensity was then converted into variations of the CMB brightness temperature using the relation $\Delta T/T_0 = \Delta I/B_\nu$, where B_ν is the blackbody intensity with temperature $T_0 = 2.725$ K.

Figure 9 shows the results of this procedure for several cases. It is most striking that the amplitude of the variable component decreases with increasing energy injection redshift. This can be understood as follow: we have seen in Sect. 5.1 and 5.2 that for very early energy injection most of the pre-recombinational emission is expected to arise at $z \sim 3000$ for hydrogen, and $z \sim 11000$ for helium, (i.e. the redshifts at which the Lyman-continuum of the considered atomic species becomes optically thick) with a typical line-width $\Delta\nu/\nu \sim 1$. In this case the total

variability of the signal is mainly due to the non-trivial superposition of many broad neighboring spectral features. Most importantly, very little variability will be added by the high redshift wing of the pre-recombinational lines and in particular the *beginning* of the injection process. This is because (i) at high z the emission is much smaller (cf. Fig. 1 and 3), and (ii) electron scattering broadens lines significantly, smoothing any broad feature even more (see Appendix A.4).

On the other hand, when the energy injection occurs at lower redshift this increases the variability of the signal because (i) electron scattering in the case of single momentary energy release does not smooth the step-like feature due to the beginning of the injection process as strongly, and (ii) the total emission amplitude and hence the step-like feature increases (see Fig 1 and 3). Once the injection occurs very close to the redshift at which the Lyman-continuum is becoming optically thick (see Sect. 5.1), i.e. where the pre-recombinational emission has an extremum, this therefore should lead to a strong increase of the variability. On the other hand, for energy injection well before this epoch the atomic transitions lead to an increase in the overall amplitude of the distortions rather than the variability.
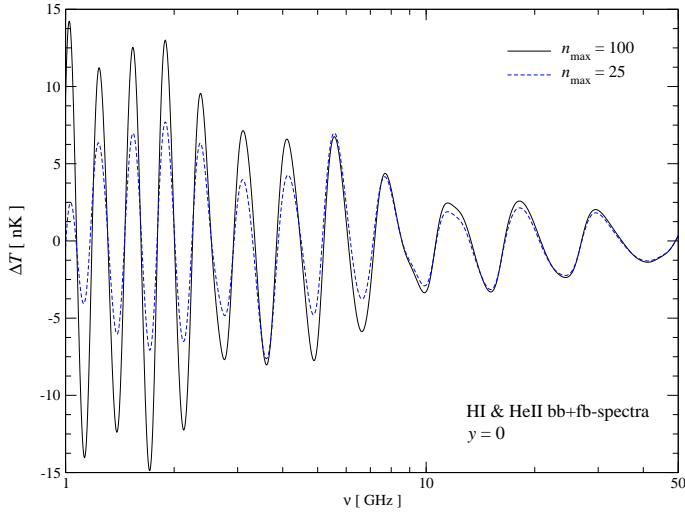
Fig. 10. Comparison of the variable component in the standard ($y = 0$) H I + He II bound-bound and free-bound recombination spectrum for $n_{max} = 100$ and 25.

Indeed this can be also seen in Fig. 9, where for $z_i = 4000$ the variable component is $\sim 3 - 8$ times larger than the normal recombinational signal, with a peak to peak amplitude of $\sim 50 - 70$ nK instead of $\sim 10 - 15$ nK at frequencies around ~ 1.5 GHz. Even for $z_i \gtrsim 15000$ the amplitude of the variable component is still $1.5 - 2$ times larger than in the case of standard recombination, but it practically does not change anymore when going to higher injection redshifts. For $z_i \sim 11000$ one expects a similarly strong increase in the variability as for $z_i \sim 4000$, but this time due to He II. In addition to the change in amplitude of the variable component, in all cases the signal is shifted with respect to the normal recombinational signal. These shifts should also make it easier to distinguish the signatures from pre-recombinational energy release from those arising because of normal recombination.

It is important to mention that the total amplitude of the variable component, should still increase when including more shells into the computation. As shown in Chluba et al. (2007a), for $y = 0$ in particular the overall level of recombinational emission at low frequencies strongly depends on the completeness of the atomic model. Similarly, the variability of the recombination spectrum changes. We illustrate this fact in Fig. 10, where we compare the variability in the H I + He II recombination spectrum for 25 shells ($y = 0$), with the one obtained in our 100 shell computations (Chluba et al. 2007a; Rubino-Martin et al. 2007). As one can see, at low frequencies ($\nu \sim 1 - 3$ GHz) the amplitude of the variable component increases by more than a factor of 2 when including 100 shells, reaching a peak to peak amplitude of ~ 30 nK. This is due to the fact that for a more complete atomic model additional electrons are able to pass through a particular transition between highly excited states.

5.3.3. Dependence of the distortion on the energy injection history

Until now we have only considered cases for single momentary energy injection. However, physically this may not be very realistic, since most of the possible injection mechanisms release energy over a more broad range of redshifts. Also the discussion in Sect. 5.3.2 has shown that for single injection a large part of the variability can be attributed to the inset of the energy release.
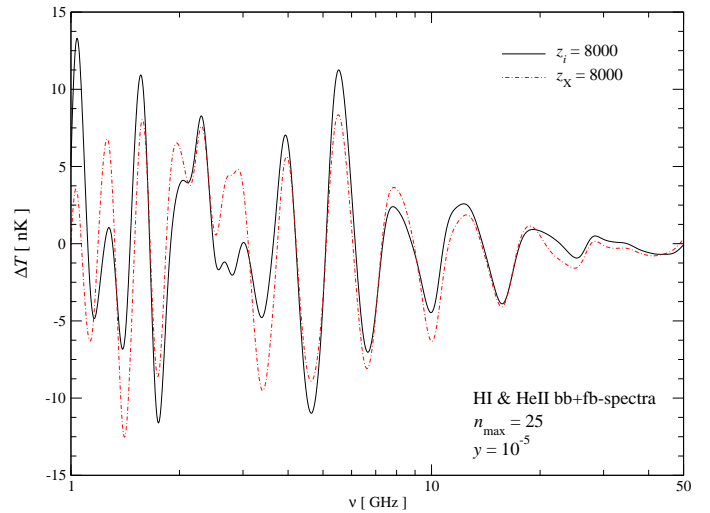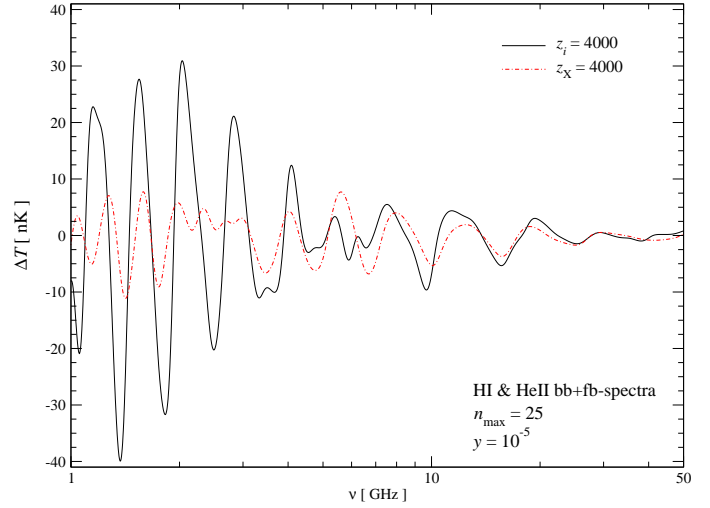

Fig. 11. Comparison of the variable component in the H I + He II bound-bound and free-bound recombination spectra for single energy injection (black solid curves) and energy injection due to long-lived decaying particles with different lifetimes (red dashed-dotted curves). In all cases the computations were performed including 25 shells and a maximal y-parameter $y = 10^{-5}$.

Therefore it is important to investigate the potential signatures of other injection mechanisms.

For the signals under discussion long lived decaying particles are most interesting. In Sect. 2.1.1 we have given some simplified analytic description of this problem. In Fig. 11 we show the variable component for the CMB spectral distortion due to the presence of hydrogen and He II at low frequencies, in the case of single injection and for energy release due to long-lived decaying particles. It is clear that for $z_X = 4000$ the variability is significantly smaller than in the case of single energy injection. This is due to the fact that the inset of the atomic transitions is much more gradual than in the case of single injection. However one should mention that for energy injection due to decaying particles the effective y-parameter at $z = 4000$ is still only $\sim 1/3$ of the maximal value, so that the level of variability cannot be directly compared with the case of single energy injection. Nevertheless, the structure of the variable component still depends non-trivially on the effective decay redshift, so that one in principle should be able to distinguish different injection scenarios.

Similarly, one could consider the case of annihilating particles. However, here energy is effectively released at higher redshifts[5] and also within a much broader redshift interval. In this case, one has to follow the evolution of the CMB spectrum due to this heating mechanism from an initial μ-type distortion to a partial y-type distortion in more detail. Also one can expect that the redistribution of photons via electron scattering will become much more important (see Appendix A.4), and that the free-free process will strongly alter the number of photons emitted via atomic transitions (see Appendix A.5). In addition, collisional processes may become significant, in particular those leading to transitions among different bound-bound level, or to the continuum, since they are not associated with the emission of photons. This problem will be left for some future work.

6. Discussion and conclusions

In the previous Sections we have shown in detail how intrinsic y-type CMB spectral distortions modify the radiation released due to atomic transitions in primordial hydrogen and He II at high redshifts. We presented the results of numerical computations including 25 atomic shells for both H I and He II, and discussed the contributions of several individual transitions in detail (e.g. see Fig. 6), also taking the broadening of lines due to electron scattering into account. As examples, we investigate the case of instantaneous energy release (Sect. 5.3.2) and exponential energy release (Sect. 5.3.3) due to long lived decaying particles, separately.

Our computations show that several additional photons are released during the pre-recombinational epoch, which in terms of number can strongly exceed those from the recombinational epoch (see Sect. 5.3.1). The number of loops per nucleus scales roughly proportional to the values of y, i.e. $\mathcal{N}_{loop}^{HI} \sim 3.2 \times [y/10^{-5}]$ and $\mathcal{N}_{loop}^{HeII} \sim 30 \times [y/10^{-5}]$ for hydrogen and He II respectively, where effectively about 3 photons per loop are emitted in the bound-bound transition.

Due to the non-trivial overlap of broad neighboring pre-recombinational lines (from bound-bound and free-bound transitions), rather narrow ($\Delta\nu/\nu \sim 0.1-0.3$) spectral features on top of a broad continuum appear, which both in shape and amplitude depend on the time-dependence of the energy injection process and the value of the intrinsic y-type CMB distortion. At high frequencies ($\nu \sim 500\,\text{GHz} - 1600\,\text{GHz}$) an emission-absorption feature is formed, which is completely absent for $y = 0$, and is mainly due to the superposition of pre-recombinational emission in the Lyman-α line, and the higher Lyman-series and Lyman continuum. Looking at Fig. 12 it becomes clear that this absorption feature (close to $\nu \sim 1400\,\text{GHz}$) in all shown cases even exceeds the intrinsic y-distortion. For $y = 10^{-5}$ it even reaches $\sim 10\%$ of the CMB blackbody intensity. Unfortunately, it appears in the far Wien-tail of the CMB spectrum, where especially the cosmic infrared background due to dusty star-forming galaxies is dominant (Fixsen et al. 1998; Lagache et al. 2005). Still one may hope to be able to extract such spectral feature in the future.

One should stress that still *all* the discussed additional pre-recombinational spectral distortions are in general *small* in comparison with the intrinsic y-distortion. As Fig. 12 shows, the amplitude of the additional distortions is typically well below 1% of the CMB y-distortion. However, at low frequencies ($\nu \sim 1\,\text{GHz}$)
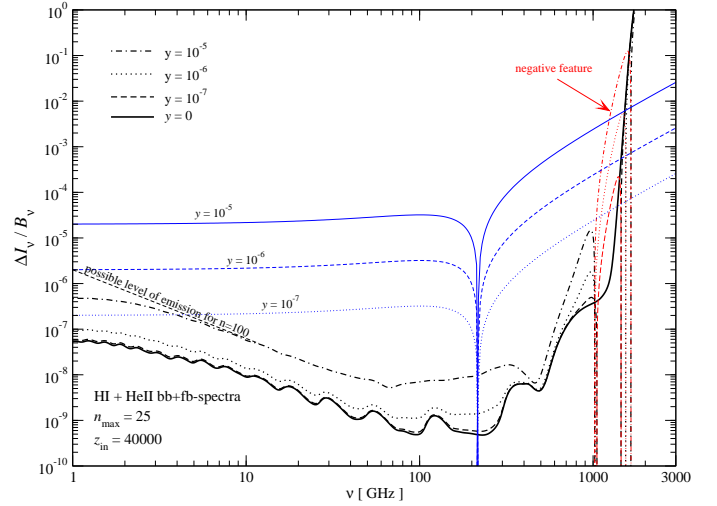
[5] This conclusion depends also on the temperature/energy dependence of the annihilation cross section. We assumed s-wave annihilation (e.g. see McDonald et al. 2001).

Fig. 12. Spectral distortions relative to the CMB blackbody spectrum, B_ν. The thin blue curves show the absolute value of a y-type distortion. At low frequencies we indicate the expected level of emission when including more shells in our computations.

the additional distortions should reach $\sim 10\%$ of the intrinsic y-distortion, and a lower frequency may even exceed it. But in this context it is more important that due to the processes discussed here new *narrow* spectral features appear, which have a unique variability (e.g. see Fig. 9), that is even stronger than in the case of the recombinational lines from standard recombination ($y = 0$). Such variability is very hard to mimic by any astrophysical foreground or systematic problem with the instruments. As emphasized earlier for the cosmological recombination spectrum (Sunyaev & Chluba 2007, 2008), this may allow us to measure them *differentially*, also making use of the fact that practically the same signal is coming from all directions on the sky. For intrinsic y-distortions direct differential measurements are much harder, since it has so broad spectrum. Furthermore, as pointed out in the introduction, by measuring the narrow spectral features under discussion one could in principle distinguish pre- and post-recombinational energy release, an observation that cannot be achieved by directly measuring the average y-distortion of the CMB.

Above it was pointed out, that there is no principle difficulty in computing the spectral distortions due to pre-recombinational atomic transitions in H I and He II for more general energy injection histories, if necessary. In particular very early injection, involving μ-type distortions, may be interesting, since stimulated emission could strongly amplify the emission a low frequencies, and hence the total number of emitted photons per atom. However, to treat this problem one has to follow the detailed evolution of the CMB spectral distortion due to the injection process (see e.g. Hu & Silk 1993a). Also the effect of electron scattering on the distortions due to the pre-recombinational atomic transitions, in particular because of the recoil effect, has to be treated more rigorously. Simple estimates show (see Appendix A.5) that at low frequencies also the modifications due to the free-free absorption will become significant. Furthermore, one has to account for collisional processes, since they should become important at very high redshifts, even for shells with rather low n.

An additional difficulty arises due to the fact that both at very low and at very high frequencies the back-reaction of the pre-recombinational distortion on the ambient radiation field may

not be negligible (see Fig. 12). This could also still affect the details of the results presented here, but the main conclusions should not change. We defer all these problems to another paper.

Appendix A: Computational details

A.1. Formulation of the problem

Details on the formulation of the problem for a pure blackbody CMB radiation field are given in Rubiño-Martín et al. (2006) and references therein. We shall use the same notation here. The main difference with respect to the standard recombination computation is due to the possibility of a *non-blackbody* ambient radiation field, which affects the net bound-bound and free-bound rates as explained in Sect. 3. Also the temperature of the electrons in general is no longer equal to the effective temperature of the photons, as we discuss below (see Sect. A.3). Since we consider only small intrinsic spectral distortions all the modification to the solution for the level populations are rather small, and most of the differences will appear only as pre-recombinational emission due to atomic transitions, but with practically no effect on the ionization history.

One additional modification is related to the Lyman-continuum. As was realized earlier (Zeldovich et al. 1968; Peebles 1968), during the recombination epochs photons cannot escape from the Lyman-continuum. However, at high redshifts the number of neutral atoms is very small, so that the Lyman-continuum becomes optically thin. In order to include the escape of photons in the Lyman-continuum we follow the analytic description of Chluba & Sunyaev (2007), in which an approximation for escape probability in the Lyman-continuum was given by

$$P_{esc}^{Ly-c}(z) \approx \frac{1}{1 + \tau_c^{esc}}, \qquad (A.1)$$

with $\tau_c^{esc} = \frac{c\,\sigma_{1sc}\,N_{1s}}{H}\frac{k_B T_e}{h\nu_c}$. Here σ_{1sc} is the threshold photoionization cross section of the 1s-state, N_{1s} is the number density of atoms in the ground state, and ν_c is the threshold frequency. For the standard cosmology the H I Lyman-continuum becomes optically thin above $z \sim 3000 - 4000$, while for He II this occurs at $z \gtrsim 12000 - 16000$. As our computations show, it is crucial to include this process, since at high redshifts almost all loops begin or terminate in the Lyman-continuum (see Sect. 5).

A.2. High redshift solution

At high redshifts, well before the actual recombination epoch of the considered atomic species, one can simplify the problem when realizing that the ionization degree is actually not changing significantly. Although the inclusion of intrinsic CMB spectral distortion does lead to some small changes in the populations with respect to the Saha values, the total number of electrons that are captured by protons and helium nuclei is tiny as compared to the total number of free electrons. Therefore one can neglect the evolution equation for the electrons, until the actual recombination epoch is entered. For H I we use this simplification until $z \sim 3500$, while for He II we follow the full system below $z \sim 20000$. Before we simply use the RECFAST-solution for N_e (Seager et al. 1999, 2000). In several different cases we checked that these settings do not affect the spectra.

Furthermore, one should mention that at high redshifts for $n > 2$ we use the variable $\Delta N_i = N_i - N_i^{2s}$ instead of N_i, since $\Delta N_i/N_i$ becomes so small. Here N_i^{2s} is the expected population of level i in Boltzmann-equilibrium relative to the 2s-level. We then change back to the variable N_i at sufficiently low redshifts.

A.3. Recombination and photoionization rates

The computation of the photoionization and recombination rates for many levels is rather time-consuming. In an earlier version of our code (Chluba et al. 2007a) we tabulated the recombination rates for all levels before the actual computation and used *detailed balance* to infer the photoionization rates. This treatment is possible as long as the photon and electron temperature do not depart significantly from each other, and when the background spectrum is given by a blackbody. Here we now generalize this procedure in order to account for the small difference in the electron and photon temperature, in particular at low redshifts ($z \lesssim 800$), and to allow for non-blackbody ambient photon distributions.

At high redshifts ($z \gtrsim 3000$) the electron temperature is always equal to the Compton equilibrium temperature (Zeldovich & Sunyaev 1969):

$$T_e^{eq} = \frac{k_B T_\gamma}{h} \frac{\int x^4 n_\gamma(x)\,dx}{4 \int x^3 n_\gamma(x)\,dx} \qquad (A.2)$$

within the given ambient radiation field. Due to the extremely high specific entropy of the Universe (there are $\sim 1.6 \times 10^9$ photons per baryon) this temperature is reached on a much shorter time-scale than the redistribution of photons via Compton scattering requires. For a μ-type distortion T_e^{eq} is always very close to the effective photon temperature, whereas for a y-type distortion with $y \ll 1$ one has $T_e \approx T_\gamma[1 + 5.4\,y]$ (Illarionov & Syunyaev 1975a). This simplifies matters, since there is no need to solve the electron temperature evolution equation, and the photoionization and recombination rates can therefore be pre-calculated.

At redshifts below $z \sim 3000$ we solve for the electron temperature accounting for the non-blackbody ambient radiation field. In this case the photon temperature inside the term due to the Compton interaction has to be replaced by T_e^{eq} as given by Eq. (A.2), such that the temperature evolution equation reads

$$\frac{\partial T_e}{\partial z} = \frac{\kappa_C\,T_\gamma^4}{H(z)[1+z]}\frac{X_e}{1 + f_{He} + X_e}\,[T_e - T_e^{eq}] + \frac{2T_e}{1+z}, \qquad (A.3)$$

where $\kappa_C = 4.91 \times 10^{-22}\ s^{-1}\,K^{-4}$.

Since for small intrinsic CMB spectral distortions the correction to solution for the temperature of the electrons is rather small, it is always possible to use the standard RECFAST solution for T_e as a reference. Tabulating *both* the photoionization and recombination rates, and their first derivatives with respect to the ratio of the electron to photon temperature $\rho = T_e/T_\gamma$, it is possible to approximate the exact rates with high accuracy using first order Taylor polynomials. To save memory, we only consider all these rates in some range of redshifts around the current point in the evolution and then update them from time to time. At high redshifts we typically used 200 points per decade in logarithmic spacing. At low redshift ($z \lesssim 5000$) we use 2 points per $\Delta z = 1$. Another improvement can be achieved by rescaling the reference solution for T_e with the true solution whenever the tabulated rates are updated. With these settings we found excellent agreement with the full computation, but at significantly lower computational cost.

A.4. Inclusion of electron scattering

As has been mentioned by Dubrovich & Stolyarov (1997) and shown more detail by Rubino-Martin et al. (2007), the broadening due to scattering of photons by free electrons has to be included for the computation of the He II recombination spectrum. Similarly, one has to account for this effect, when computing the spectral distortions arising from higher redshifts. Here we only consider redshifts $z \lesssim 5 \times 10^4$, and hence the electron scattering Compton-y-parameter[6]

$$y_e(z) = \int_0^z \frac{kT_e}{m_e c^2} \frac{c\,N_e\,\sigma_T}{H(z')(1+z')}\,dz' \approx 4.8 \times 10^{-11}\,[1+z]^2 \qquad (A.4)$$

is smaller than ~ 0.12, so that the line-broadening due to the Doppler-effect is significant ($\Delta\nu/\nu|_{Doppler} \sim 0.58$), but still rather moderate in comparison with the width of the quasi-continuous spectral features, arising from high redshifts (see Sect. 5.1 and 5.2). However, already at $z \lesssim 2.5 \times 10^4$ one has $y_e \lesssim 0.03$, such that $\Delta\nu/\nu|_{Doppler} \lesssim 0.29$.

Regarding the line-shifts due to the recoil-effect one finds that they are not very important, since even for the H I Lyman-continuum one has $\Delta\nu/\nu|_{recoil} \lesssim -0.14$ at $z \lesssim 5 \times 10^4$. Although for the He II Lyman-continuum the shifts due to the recoil-effect is four times larger, we shall not include it in our results. One therefore expects that at frequencies $\nu \gtrsim 57$ GHz the presented distortions may still be modified due to this process, but we will consider this problem in a future paper.

For the bound-bound spectrum we follow the procedure described in Rubino-Martin et al. (2007), where the resulting spectral distortion at observing frequency ν for one particular transition is given by (see also Zeldovich & Sunyaev 1969)

$$\Delta I_{ij}(\nu)\big|_{Doppler} = \int \frac{\nu^3}{\nu_0^3} \frac{\Delta I_{ij}(\nu_0)}{\sqrt{4\pi y_e}} \times e^{-\frac{(\ln[\nu/\nu_0]+3y_e)^2}{4y_e}}\,\frac{d\nu_0}{\nu_0}. \qquad (A.5)$$

---

[6] Note that y_e differs from y as defined in Eq. (1), since it describes the redistribution of some photon over frequency because of electron scattering rather than the global energy exchange with the ambient blackbody radiation field.

Here $\Delta I_{ij}(\nu_0)$ denotes the spectral distortion for the considered transition evaluated at frequency ν_0 and computed without the inclusion of electrons scattering (e.g. see Rubiño-Martín et al. 2006), but accounting for the non-blackbody ambient radiation field. Note that $y_e(z)$ has to be calculated starting at the emission redshift $z_{em} = \nu_{ij}/\nu_0 - 1$, where ν_{ij} is the transition frequency.

For the spectral distortion resulting from the free-bound transitions one in addition has to include the frequency-dependence of the photoionization cross section. We shall neglect the line broadening because of electrons scattering for the moment. Then, following Chluba & Sunyaev (2006) and using the definitions of Sect. 3.2, in the optically thin limit the spectral distortion of the CMB at observing frequency ν due to direct recombinations to level i is given by

$$\Delta I_{ic}(\nu) = \frac{2h\nu^3}{c^2} \int_{z_t}^{\infty} n_\gamma(\nu_z, z) \frac{cN_i \, \sigma_i(\nu_z)}{H(z)(1+z)}$$
$$\times \left[\frac{N_e N_p}{N_i} \tilde{f}_i(T_e) \, e^{x_z + \mu(x_z) + [x_{ic} - x_z]/\rho} - 1 \right] dz, \qquad (A.6)$$

with $\nu_z = \nu(1+z)$, $1 + z_t = \nu_{ic}/\nu$ and $x_z = h\nu_z/kT_\gamma \equiv h\nu/kT_0$. Furthermore, $n_\gamma(\nu_z, z)$ denotes the intrinsic CMB occupation number at redshift z including the spectral distortion and evaluated at frequency ν_z. For the Lyman-continuum one would in addition multiply the integrand of Eq. (A.6) by $P_{esc}^{Ly-c}(z)$, to obtain the approximate solution for the resulting distortion.

Now, to include the broadening because of scattering by electrons one has to solve the 2-dimensional integral

$$\Delta I_{ic}(\nu)|_{Doppler} = \frac{2h\nu^3}{c^2} \int_0^{\infty} dz \int \frac{\Delta n(\tilde{\nu}_z, z)}{\sqrt{4\pi y_e}} e^{-\frac{(\ln[\nu/\tilde{\nu}] + 3y_e)^2}{4y_e}} \frac{d\tilde{\nu}}{\tilde{\nu}}, \qquad (A.7)$$

where $\tilde{\nu}_z = \tilde{\nu}(1+z)$ and

$$\Delta n(\nu, z) = n_\gamma(\nu, z) \frac{cN_i \, \sigma_i(\nu)}{H(z)(1+z)} \left[\frac{N_e N_p}{N_i} \tilde{f}_i(T_e) \, e^{x + \mu(x) + [x_{ic} - x]/\rho} - 1 \right]. \qquad (A.8)$$

In the numerical evaluation of these integrals it is advisable to make use of the knowledge about the integrand, since otherwise they may converge very slowly.

A.5. Estimate regarding the free-free process

The free-free optical depth, τ_{ff}, is given by

$$\tau_{ff}(x, z, z_f) = \int_z^{z_f} K_{ff}(x, z') \frac{N_e \, \sigma_T \, c \, dz'}{H(z')(1+z')}, \qquad (A.9)$$

Here N_e is the free electron number density and $H(z)$ is the Hubble factor, which in the radiation dominated era ($z \gtrsim 3300$) is given by $H(z) \approx 2.1 \times 10^{-20} [1 + z]^2 \, s^{-1}$. The free-free absorption coefficient $K_{ff}(x, z)$ is given by

$$K_{ff}(x, z) = \frac{\alpha \lambda_e^3}{2\pi \sqrt{6\pi}} \frac{[1 - e^{-x}]}{x^3 \theta_\gamma^{7/2}} N_b \, g_{ff}^{H^+}(x, \theta_\gamma), \qquad (A.10)$$

where $\lambda_e = h/m_e c = 2.426 \times 10^{-10}$ cm is the Compton wavelength of the electron, $\alpha \approx 1/137$ is the fine structure constant, $g_{ff}^{H^+}$ is the free-free Gaunt factor for hydrogen. We also introduced the dimensionless temperature of the photon field $\theta_\gamma = k_B T_\gamma/m_e c^2 \approx 4.6 \times 10^{-10} [1 + z]$. For simplicity we again shall assume $T_e \equiv T_\gamma$. Furthermore we approximated the He^{++} free-free Gaunt factor by $g_{ff}^{He^{++}} \approx 4g_{ff,p}$ and assumed that $z \gtrsim 8000$, since in the considered frequency range most of the free-free absorption occurs well before $He\,III \rightarrow He\,II$ recombination (see below).

Using the condition $\tau_{ff} \approx 1$ one can estimate the frequency $x_{ff}(z)$, below which one expects free-free absorption to become important. Since at $z \gtrsim 8000$ all the atoms are ionized, the number density of free electrons is given by $N_e = (1 - Y_p/2) N_b \approx 2.2 \times 10^{-7} (1 + z)^3$ cm^{-3}. Here we used $N_{b,0} = 2.5 \times 10^{-7}$ cm^{-3} as the present day baryon number density. For $x_{ff} \ll 1$ one then finds $\tau_{ff}(x, z = 0, z_{em}) \approx 9.6 \times 10^{-7} [g_{ff}/5] \sqrt{1 + z_{em}} \, x^{-2}$, where z_{em} is the redshift of emission. Here we are only interested in photons that can be observed at $x \gtrsim 0.02$, i.e. $\nu \gtrsim 1$ GHz today. At this frequency $\tau_{ff} \gtrsim 1$ for $z_{em} \gtrsim 1.7 \times 10^5$. Below this redshift one can neglect the free-free process in the computation of the bound-bound and free-bound spectra. However, a more complete treatment will be presented in a future paper.

Assuming that $z_{em} \sim 8000$ one finds that $\tau_{ff} \lesssim 0.21$ for $x \gtrsim 0.02$. This justifies the approximations that were made above, since the contributions to the free-free optical depth coming from $z \lesssim 8000$ are not very large.

Appendix B: Analytic solution

B.1. The 2-shell atom

Including only 2 shells one can analytically derive the solution for the Lyman-α line under quasi-stationary evolution of the populations. For this we need to determine the net radiative rate, $\Delta R_{Ly\alpha} = A_{21}(1 + n_{21}) N_{2p}[1 - wN_{1s}/N_{2p} \times n_{21}/(1 + n_{21})]$, with $w = 3$ and $n_{21} = n_\gamma(\nu_{21}, T_\gamma)$. The ratio $\Lambda = n_{21}/(1 + n_{21})$ is directly determined by the given ambient radiation field including the spectral distortion. Since the distortions are considered to be small we can use $A_{21}(1 + n_{21}) N_{2p} \approx A_{21}(1 + n_{21}^{eq})N_{2p}^{eq}$ for the term in front of the brackets. Here n_{21}^{eq} and N_{2p}^{eq} are equilibrium values for the photon occupation number and the 2p-population, respectively. Therefore we only have to determine the ratio $\xi = wN_{1s}/N_{2p}$ in order to compute the Lyman-α line intensity analytically.

We shall first consider the case of hydrogen at high redshifts ($z \gtrsim 3000 - 4000$). There the escape probability in the H I Lyman-α line and the H I Lyman-continuum are very close to unity. Therefore the 2s-1s-two-photon transition does not play any important role in defining the number density of atoms in the ground state. Furthermore, one can assume that the 2s-population is always in Saha-equilibrium with the continuum, and hence $N_{2s} \approx N_e N_p \, \alpha_{2s}/\beta_{2s}$ where even $N_p \approx N_H$, since the total fraction of neutral atoms is tiny.

For the 1s- and 2p-states the rate equations read

$$N_e N_p \, \alpha_{1s} - \frac{\xi \beta_{1s}}{w} N_{2p} + A_{21}(1 + n_{21}) N_{2p}[1 - \xi\Lambda] \approx 0 \qquad (B.1a)$$

$$N_e N_p \, \alpha_{2p} - \beta_{2p} N_{2p} - A_{21}(1 + n_{21}) N_{2p}[1 - \xi\Lambda] \approx 0, \qquad (B.1b)$$

where we substituted $N_{1s} = \xi N_{2p}/w$ and $\Lambda = n_{21}/(1 + n_{21})$. Solving this system with[7] $N_p \approx N_H$ for ξ one finds

$$\xi = \frac{\alpha_{1s}\beta_{2p} + A_{21}(\alpha_{1s} + \alpha_{2p})[1 + n_{21}]}{\alpha_{2p}\beta_{1s}/w + A_{21}(\alpha_{1s} + \alpha_{2p}) n_{21}}. \qquad (B.2)$$

With appropriate replacements the same expression can be used to compute the He II Lyman-α line.

B.1.1. Including the Lyman-α and continuum escape

In order to include the escape probability in the Lyman-α line, P_{21}, and the Lyman-continuum, P_{1c}, one simply should replace $A_{21} \rightarrow P_{21} A_{21}$, $\alpha_{1s} \rightarrow P_{1c}\alpha_{1s}$ and $\beta_{1s} \rightarrow P_{1c}\beta_{1s}$, where the escape probabilities can be computed using equilibrium values for N_{1s} and N_{2p}. As long as the 2s-1s-two-photon transition can be neglected this yields a very accurate approximation for the Lyman-α line (cf. Sects. 5.1).

Around the region where the Lyman-continuum is becoming optically thick ($z \sim 3000$ for H I and $z \sim 11000$ for He II), for simple estimates one can use

$$\tau_{Ly-c}^{esc} \approx \begin{cases} 7.2 \times 10^{-24} \, e^{x_{1s}} \, [1+z]^4 & \text{for H I} \\ 3.1 \times 10^{-24} \, e^{x_{1s}} \, [1+z]^{7/2} & \text{for He II} \end{cases} \qquad (B.3)$$

$$\tau_{Ly\alpha}^{esc} \approx \begin{cases} 3.0 \times 10^{-19} \, e^{x_{1s}} \, [1+z]^3 & \text{for H I} \\ 5.0 \times 10^{-19} \, e^{x_{1s}}[1 - e^{-3x_{1s}/4}] \, [1+z]^{5/2} & \text{for He II} \end{cases}, \qquad (B.4)$$

with $x_{1s} \approx 5.79 \times 10^4 \, Z^2[1 + z]^{-1}$.

B.1.2. More approximate behavior

In order to understand the solution for the H I Lyman-α line we now turn to the corresponding intensity as a function of redshift (Rubiño-Martín et al. 2006, e.g.). This yields

$$\Delta I_\nu = \frac{hc}{4\pi} \frac{\Delta R_{Ly\alpha}(z)}{H(z)[1+z]^3} = \frac{hc}{4\pi} \frac{A_{21}(1 + n_{21}) N_{2p}[1 - \xi\Lambda]}{H(z)[1+z]^3}. \qquad (B.5)$$

Using the approximation (B.2) for ξ one can then find

$$1 - \xi\Lambda \approx \frac{\alpha_{2p}\beta_{1s}/w (1 + n_{21}) - \alpha_{1s}\beta_{2p} n_{21}}{[\alpha_{2p}\beta_{1s}/w + A_{21}(\alpha_{1s} + \alpha_{2p}) n_{21}](1 + n_{21})}. \qquad (B.6)$$

With this one then has

$$\Delta I_\nu \approx \frac{hc}{4\pi} \frac{A_{21} N_{2p}}{H(z)[1+z]^3} \frac{\alpha_{2p}\beta_{1s} (1 + n_{21})}{\alpha_{2p}\beta_{1s} + w A_{21}(\alpha_{1s} + \alpha_{2p}) n_{21}}$$
$$\times \left[1 - w \frac{\alpha_{1s}\beta_{2p}}{\alpha_{2p}\beta_{1s}} e^{-(x_{21} + \mu_{21})} \right]. \qquad (B.7)$$

Here we used $x_{21} = h\nu_{21}/kT_\gamma$ and $(1 + n_{21})/n_{21} = e^{x_{21} + \mu_{21}}$, with the frequency dependent chemical potential $\mu_{21} = \mu(x_{21})$.

---

[7] Note that even if one (more correctly) uses $N_p = N_H - N_{1s} - N_{2s} - N_{2p}$ in Eq. (B.1) the solution for ξ does not change.

First factor

We can now simplify the expression (B.7) when realizing that except for the term inside brackets, in the case of small intrinsic CMB spectral distortions, one can just use equilibrium values. At high redshifts one has $H(z) \propto (1 + z)^2$. Furthermore $N_{2p}^{eq} \approx 3 N_{1s}^{eq} e^{-x_{21}} \approx 3 N_e N_H \alpha_{1s}^{eq} e^{-x_{21}} / \beta_{1s}^{eq}$ and $\beta_i^{eq} = \alpha_i^{eq} e^{-x_{ic}} / \tilde{f}_i(T_e)$. Also with rather high accuracy one finds $\alpha_{2p}^{eq} \approx \alpha_{1s}^{eq}/3$ and $\frac{\alpha_{2p}\beta_{1s}}{w} \ll A_{21}(\alpha_{1s} + \alpha_{2p}) n_{21}$, so that

$$F(z) = \frac{h c}{4\pi} \frac{A_{21} N_{2p}}{H(z)[1 + z]^3} \frac{\alpha_{2p}\beta_{1s} (1 + n_{21})}{\alpha_{2p}\beta_{1s} + w A_{21}(\alpha_{1s} + \alpha_{2p}) n_{21}}$$

$$\approx \frac{h c}{4\pi} \frac{3 N_e N_H}{H(z)[1 + z]^3} \frac{\alpha_{2p}^{eq}}{4 + \tau_{Ly-c}^{esc}} \propto \frac{(1 + z)^{1/2}}{4 + \tau_{Ly-c}^{esc}}. \tag{B.8}$$

Here we have also included the escape probabilities in the Lyman-α line and continuum as explained in Appendix B.1.1. Note that the Lyman-α escape probability drops out of the expression, so that only the Lyman-continuum escape probability is strongly affecting the pre-recombinational line shape. We have also used $\alpha_i^{eq} = \frac{8\pi}{c^2} \tilde{f}_i(T_e) e^{x_{ic}} I_i^{eq}$, with the integral

$$I_i^{eq} = \int_{\nu_{ic}}^{\infty} \frac{\nu^2 \sigma_i(\nu)}{e^x - 1} d\nu \approx \sigma_i(\nu_{ic}) \nu_{ic}^3 M_{-1}(x_{ic}), \tag{B.9a}$$

where we have assumed $\sigma_i(\nu) \approx \sigma_i(\nu_{ic}) \frac{\nu_{ic}^3}{\nu^3}$. The integral $M_i(x)$ is defined and discussed in Appendix C. For the 2p-state one has $\sigma_{2p}(\nu_{2pc}) \nu_{2pc}^3 \approx 7.54 \times 10^{27} Z^4 \text{ cm}^{-2} \text{ s}^{-3}$.

We checked the scaling of F numerically and found

$$F(z) \approx 5.6 \times 10^{-26} \frac{(1 + z)^{1/2}}{1 + \tau_{Ly-c}^{esc}/4} \text{ J m}^{-2} \text{ s}^{-1} \text{ Hz}^{-1} \text{ sr}^{-1} \tag{B.10}$$

within $\lesssim 20\%$ accuracy in the important redshift range.

Second factor

Using the definitions of α_i and β_i as given in Sect. 3.1 and 3.2 one directly finds $w \frac{\alpha_{1s}\beta_{2p}}{\alpha_{2p}\beta_{1s}} e^{-(x_{21}+\mu_{21})} \equiv e^{-\mu_{21}} G(z)$ with

$$G(z) = \frac{\left\langle n e^{\mu(x)+(x_{1sc}-x)\Delta\rho/\rho} \right\rangle_{1s} \langle n \rangle_{2p}}{\left\langle n e^{\mu(x)+(x_{2pc}-x)\Delta\rho/\rho} \right\rangle_{2p} \langle n \rangle_{1s}}. \tag{B.11}$$

Here $\Delta\rho = 1 - \rho$ and we introduced the notation

$$\langle f(\nu) \rangle_i = \int_{x_{ic}}^{\infty} \nu^2 \sigma_i(\nu) f(\nu) d\nu \tag{B.12}$$

for the average of some function $f(\nu)$ over the photoionization cross-section of level i.

In full thermodynamic equilibrium one has $G^{eq}(z) \equiv 1$, a property that can be verified using Eq. (B.11) with $\mu = 0$ and $\rho = 1$, since then $\left\langle n e^{\mu(x)+(x_{ic}-x)\Delta\rho/\rho} \right\rangle_i \equiv \langle n_{pl} \rangle_i$. Therefore we can write $G = 1 + \Delta G$. Using $\langle f \rangle_i = \langle f^{eq} \rangle_i + \langle \Delta f \rangle_i$, for small intrinsic CMB distortions (i.e. $\langle \Delta f \rangle_i / \langle f \rangle_i \ll 1$) one finds

$$\Delta G \approx \frac{\left\langle n_{pl} [\mu - \mu_{1s}^\rho] \right\rangle_{1s}}{\langle n_{pl} \rangle_{1s}} - \frac{\left\langle n_{pl} [\mu - \mu_{2p}^\rho] \right\rangle_{2p}}{\langle n_{pl} \rangle_{2p}}, \tag{B.13}$$

where $\mu_i^\rho = (x - x_{ic})\Delta\rho/\rho$. Putting things together we then have

$$1 - w \frac{\alpha_{1s}\beta_{2p}}{\alpha_{2p}\beta_{1s}} e^{-(x_{21}+\mu_{21})}$$

$$\approx \mu_{21} + \frac{\left\langle n_{pl} \mu \right\rangle_{2p}}{\left\langle n_{pl} \right\rangle_{2p}} - \frac{\left\langle n_{pl} \mu \right\rangle_{1s}}{\left\langle n_{pl} \right\rangle_{1s}}$$

$$- \frac{\left\langle n_{pl} \mu_{2p}^\rho \right\rangle_{2p}}{\left\langle n_{pl} \right\rangle_{2p}} + \frac{\left\langle n_{pl} \mu_{1s}^\rho \right\rangle_{1s}}{\left\langle n_{pl} \right\rangle_{1s}} \tag{B.14a}$$

$$\approx \mu_{21} + \mu_{2pc} - \mu_{1sc}, \tag{B.14b}$$

To lowest order, Eq. (B.14b) shows that the main reason for the emission in the Lyman-α line is the deviation of the effective chemical potential from zero at the Lyman-α resonance, and the Lyman- and Balmer-continuum frequency. However, the averages over the photoionization cross-section still lead to some notable corrections, so that also the small difference in the electron and photon temperature plays a role.

If we again use the Kramers-approximation for the photoionization cross-section, $\sigma_i(\nu) \approx \sigma_i(\nu_{ic}) \frac{\nu_{ic}^3}{\nu^3}$, looking at Eq. (3) for μ in the case of a small y-type distortion, one can write

$$\left\langle n_{pl} \right\rangle_i \approx \kappa_i M_{-1}(x_{ic}) \tag{B.15a}$$

$$\left\langle n_{pl} \mu \right\rangle_i \approx \kappa_i y [4 M_0(x_{ic}) - S(x_{ic})] \tag{B.15b}$$

$$\left\langle n_{pl} \mu_i^\rho \right\rangle_i \approx \kappa_i \frac{\Delta\rho}{\rho} [M_0(x_{ic}) - x_{ic} M_{-1}(x_{ic})], \tag{B.15c}$$

where $\kappa_i = \text{const}$ and the integrals S and M_0 are defined in Appendix C. Keeping only the leading order terms, we have

$$1 - w \frac{\alpha_{1s}\beta_{2p}}{\alpha_{2p}\beta_{1s}} e^{-(x_{21}+\mu_{21})}$$

$$\approx -y x_{1sc} \left[6.3 - 0.9375 x_{1sc} + 4.7 e^{-x_{1sc}} - 1.175 e^{-x_{1sc}/4} \right]$$

$$+ y x_{21} \left[9.4 - x_{21} \frac{e^{x_{21}} + 1}{e^{x_{21}} - 1} \right]. \tag{B.16a}$$

It is important to mention that this is still a rather rough approximation, since already applying the Kramers-formula for the photoionization cross-section introduces some significant simplification. However, this approximation may be useful for simple estimates.

Appendix C: Some integrals

C.1. Integrals M_i

In the evaluation of the recombination and photoionization rates, integrals of the form $M_i = \int_{x_{ic}}^{\infty} x^i dx/[e^x - 1]$ appear. Below we now discuss those which are of importance for us here.

C.1.1. Integral M_{-1}

For $i = -1$ one can write

$$\int_{x_{ic}}^{\infty} \frac{dx}{x[e^x - 1]} = \sum_{k=1}^{\infty} \text{Ei}(kx_{ic}) \overset{h\nu_{ic} \gg kT_\gamma}{\approx} \frac{e^{-x_{ic}}}{x_{ic}} \tag{C.1a}$$

$$\overset{h\nu_{ic} \leq kT_\gamma}{\approx} \frac{1}{x_{ic}} \left[1 - \frac{11 - 6\gamma}{12} x_{ic} - \frac{x_{ic}^2}{12} + \frac{x_{ic}}{2} \ln(x_{ic}) \right], \tag{C.1b}$$

where $\gamma \approx 0.5772$ is the Euler constant and we made used of the exponential integral $\text{Ei}(x) = \int_x^{\infty} e^{-t} dt/t$. In the limit $h\nu_{ic} \leq kT_\gamma$ the given approximation is accurate to better than 1%. For $h\nu_{ic} \geq kT_\gamma$ the first five terms in the full sum also yield similar accuracy.

Since $x_{ic} \approx 5.79 \times 10^4 Z^2 n^{-2} [1 + z]^{-1}$, it is clear that at $z \lesssim 1.45 \times 10^4 Z^2$ both Lyman- and Balmer-continuum are still in the exponential tail of the CMB blackbody. In the redshift range $1.45 \times 10^4 Z^2 \lesssim z \lesssim 5.79 \times 10^4 Z^2$ the Lyman-continuum is still in the exponential tail of the CMB, while the Balmer-continuum is already in the Rayleigh-Jeans part of the spectrum. Only at $z \gtrsim 5.79 \times 10^4 Z^2$ one can use the low frequency expansion of Eq. (B.9) for both cases. However, to within $\lesssim 30\%$ one may also apply Eq. (C.1a) in the whole range.

C.1.2. Integral M_0

For $i = 0$ one can write

$$M_0 = \int_{x_{ic}}^{\infty} dx/[e^x - 1] = \sum_{k=1}^{\infty} \int_{x_{ic}}^{\infty} e^{-kx} dx = \sum_{k=1}^{\infty} e^{-kx_{ic}}/k$$

$$= x_{ic} - \ln(e^{x_{ic}} - 1), \tag{C.2}$$

which for $x_{ic} \lesssim 1$ can be approximated as $M_0 \approx \frac{x_{ic}}{2} - \frac{x_{ic}^2}{24} - \ln(x_{ic})$, while for $x_{ic} \gg 1$ one has $M_0 \approx e^{-x_{ic}} [1 + e^{-x_{ic}}/2]$.

C.2. Integral S

In the evaluation of the recombination and photoionization rates one also encounters $S(x) = \int_{x_{ic}}^{\infty} dx\, x\, \frac{e^x+1}{[e^x-1]^2}$. The first part of this integral, $\propto x e^x/[e^x-1]^2$, can be directly taken yielding $\int_{x_{ic}}^{\infty} dx\, x e^x/[e^x-1]^2 = x_{ic} e^{x_{ic}}/[e^{x_{ic}}-1] - \ln(e^{x_{ic}}-1)$. Introducing the polylogarithm $\mathrm{Li}_n(x) = \sum_{k=1}^{\infty} x^k/k^n$ and realizing $x/[e^x-1]^2 = \sum_{k=1}^{\infty} k\, x\, e^{-(k+1)x}$ one can find

$$S(x_{ic}) = x_{ic}\, \frac{e^{x_{ic}}+1}{e^{x_{ic}}-1} + x_{ic}(1-x_{ic})$$
$$- (2-x_{ic})\ln(e^{x_{ic}}-1) - \mathrm{Li}_2(e^{-x_{ic}})$$

$$\overset{h\nu_{ic} \gtrsim kT_\gamma}{\underset{\approx}{\downarrow}} \sum_{k=1}^{m\approx 5} \frac{2k-1}{k^2}\, [1+k\, x_{ic}]\, e^{-k x_{ic}} \qquad (C.3a)$$

$$\overset{h\nu_{ic} \lesssim kT_\gamma}{\underset{\approx}{\downarrow}} 2 - \frac{\pi^2}{6} + x_{ic} - \frac{x_{ic}^2}{6} - 2\ln(x_{ic})\,, \qquad (C.3b)$$

The given approximations are accurate to $\lesssim 1\%$.

References

Bennett, C. L., Halpern, M., Hinshaw, G., et al. 2003, ApJS, 148, 1
Burigana, C., Danese, L., & de Zotti, G. 1991a, ApJ, 379, 1
Burigana, C., Danese, L., & de Zotti, G. 1991b, A&A, 246, 49
Burigana, C., de Zotti, G., & Danese, L. 1995, A&A, 303, 323
Burigana, C. & Salvaterra, R. 2003, MNRAS, 342, 543
Cen, R. & Ostriker, J. P. 1999, ApJ, 514, 1
Chan, K. L., Grant, C., & Jones, B. J. T. 1975, ApJ, 195, 1
Chluba, J., Rubiño-Martín, J. A., & Sunyaev, R. A. 2007a, MNRAS, 374, 1310
Chluba, J., Sazonov, S. Y., & Sunyaev, R. A. 2007b, A&A, 468, 785
Chluba, J. & Sunyaev, R. A. 2004, A&A, 424, 389
Chluba, J. & Sunyaev, R. A. 2006, A&A, 458, L29
Chluba, J. & Sunyaev, R. A. 2007, A&A, 475, 109
Chluba, J. & Sunyaev, R. A. 2008, A&A, 478, L27
da Silva, A. C., Barbosa, D., Liddle, A. R., & Thomas, P. A. 2000, MNRAS, 317, 37
Daly, R. A. 1991, ApJ, 371, 14
Danese, L. & de Zotti, G. 1982, A&A, 107, 39
Dubrovich, V. K. 1975, Soviet Astronomy Letters, 1, 196
Dubrovich, V. K. & Stolyarov, V. A. 1995, A&A, 302, 635
Dubrovich, V. K. & Stolyarov, V. A. 1997, Astronomy Letters, 23, 565
Fixsen, D. J., Cheng, E. S., Gales, J. M., et al. 1996, ApJ, 473, 576
Fixsen, D. J., Dwek, E., Mather, J. C., Bennett, C. L., & Shafer, R. A. 1998, ApJ, 508, 123
Fixsen, D. J. & Mather, J. C. 2002, ApJ, 581, 817
Hu, W., Scott, D., & Silk, J. 1994, ApJ, 430, L5
Hu, W. & Silk, J. 1993a, Phys. Rev. D, 48, 485
Hu, W. & Silk, J. 1993b, Physical Review Letters, 70, 2661
Illarionov, A. F. & Syunyaev, R. A. 1975a, Soviet Astronomy, 18, 413
Illarionov, A. F. & Syunyaev, R. A. 1975b, Soviet Astronomy, 18, 691
Kaplan, S. A. & Pikelner, S. B. 1970, The interstellar medium (Cambridge: Harvard University Press, 1970)
Kogut, A., Fixsen, D., Fixsen, S., et al. 2006, New Astronomy Review, 50, 925
Kogut, A., Fixsen, D. J., Levin, S., et al. 2004, ApJS, 154, 493
Lagache, G., Puget, J.-L., & Dole, H. 2005, ARA&A, 43, 727
Lightman, A. P. 1981, ApJ, 244, 392
Lyubarsky, Y. E. & Sunyaev, R. A. 1983, A&A, 123, 171
Markevitch, M., Blumenthal, G. R., Forman, W., Jones, C., & Sunyaev, R. A. 1991, ApJ, 378, L33
Mather, J. C., Fixsen, D. J., Shafer, R. A., Mosier, C., & Wilkinson, D. T. 1999, ApJ, 512, 511
McDonald, P., Scherrer, R. J., & Walker, T. P. 2001, Phys. Rev. D, 63, 023001
Miniati, F., Ryu, D., Kang, H., et al. 2000, ApJ, 542, 608
Oh, S. P., Cooray, A., & Kamionkowski, M. 2003, MNRAS, 342, L20
Peebles, P. J. E. 1968, ApJ, 153, 1
Roncarelli, M., Moscardini, L., Borgani, S., & Dolag, K. 2007, MNRAS, 378, 1259
Rubiño-Martín, J. A., Chluba, J., & Sunyaev, R. A. 2006, MNRAS, 371, 1939
Rubino-Martin, J. A., Chluba, J., & Sunyaev, R. A. 2007, ArXiv e-prints, 711
Salvaterra, R. & Burigana, C. 2002, MNRAS, 336, 592
Seager, S., Sasselov, D. D., & Scott, D. 1999, ApJ, 523, L1
Seager, S., Sasselov, D. D., & Scott, D. 2000, ApJS, 128, 407
Spergel, D. N., Verde, L., Peiris, H. V., et al. 2003, ApJS, 148, 175
Sunyaev, R. A. & Chluba, J. 2007, ArXiv e-prints, 710
Sunyaev, R. A. & Chluba, J. 2008, ArXiv e-prints, 802
Sunyaev, R. A. & Zeldovich, I. B. 1980, ARA&A, 18, 537
Sunyaev, R. A. & Zeldovich, Y. B. 1970a, Ap&SS, 9, 368
Sunyaev, R. A. & Zeldovich, Y. B. 1970b, Ap&SS, 7, 20
Sunyaev, R. A. & Zeldovich, Y. B. 1970c, Comments on Astrophysics and Space Physics, 2, 66
Sunyaev, R. A. & Zeldovich, Y. B. 1972a, A&A, 20, 189
Sunyaev, R. A. & Zeldovich, Y. B. 1972b, Comments on Astrophysics and Space Physics, 4, 173
Thorne, K. S. 1981, MNRAS, 194, 439
Zeldovich, Y. B., Illarionov, A. F., & Syunyaev, R. A. 1972, Soviet Journal of Experimental and Theoretical Physics, 35, 643
Zeldovich, Y. B., Kurt, V. G., & Syunyaev, R. A. 1968, Zhurnal Eksperimentalnoi i Teoreticheskoi Fiziki, 55, 278
Zeldovich, Y. B. & Sunyaev, R. A. 1969, Ap&SS, 4, 301